

# A Volume-Limited Survey of mCP Stars Within 100pc I: Fundamental Parameters and Chemical Abundances

J. Sikora,<sup>1,2</sup> G. A. Wade,<sup>2</sup> J. Power,<sup>1,2,4</sup> C. Neiner<sup>3</sup>

<sup>1</sup>*Department of Physics, Engineering Physics & Astronomy, Queen's University, Kingston, ON Canada, K7L 3N6*

<sup>2</sup>*Department of Physics and Space Science, Royal Military College of Canada, PO Box 17000 Kingston, Ontario K7K 7B4, Canada*

<sup>3</sup>*LESIA, Observatoire de Paris, PSL University, CNRS, Sorbonne Universit, Univ. Paris Diderot, Sorbonne Paris Cit,  
5 place Jules Janssen, 92195 Meudon, France*

<sup>4</sup>*Large Binocular Telescope Observatory, 933 North Cherry Avenue, Tucson, AZ 85721, USA*

Accepted 2018 Nov. 13

## ABSTRACT

We present the first results of a volume-limited survey of main sequence (MS) magnetic chemically peculiar (mCP) stars. The sample consists of all identified intermediate-mass MS stars (mCP and non-mCP) within a heliocentric distance of 100 pc as determined using Hipparcos parallaxes. The two populations are compared in order to determine the unique properties that allow a small fraction of MS stars with masses  $\gtrsim 1.4 M_{\odot}$  to host strong, large scale magnetic fields. A total of 52 confirmed mCP stars are identified using published magnetic, spectroscopic, and photometric observations along with archived and newly obtained spectropolarimetric (Stokes  $V$ ) observations. We derive the fundamental parameters (effective temperatures, luminosities, masses, and evolutionary states) of the mCP and non-mCP populations using homogeneous analyses. A detailed analysis of the mCP stars is performed using the LLMODELS code, which allows observed spectral energy distributions to be modeled while incorporating chemical peculiarities and magnetic fields. The surface gravities and mean chemical abundances are derived by modelling averaged spectra using the GSSP and ZEEMAN spectral synthesis codes. Masses and stellar ages are derived using modern, densely calculated evolutionary model grids. We confirm a number of previously reported evolutionary properties associated with mCP stars including a conspicuously high incidence of middle-aged MS stars with respect to the non-mCP subsample; the incidence of mCP stars is found to sharply increase with mass from 0.3 per cent at  $1.5 M_{\odot}$  to  $\approx 11$  per cent at  $3.8 M_{\odot}$ . Finally, we identify clear trends in the mean photospheric chemical abundances with stellar age.

**Key words:** Stars: early-type, Stars: chemically peculiar, Stars: magnetic

## 1 INTRODUCTION

Various studies of magnetic chemically peculiar (mCP) stars have been carried out over the past several decades revealing a wide range of characteristic properties. As their name suggests, these objects are defined by (1) the presence of enhanced or deficient abundances of specific elements (relative to solar abundances) that are often inhomogeneously distributed within their atmospheres and (2) by the presence of strong, large-scale surface magnetic fields (typically  $\gtrsim 100$  G, e.g. Landstreet 1982; Aurière et al. 2007) that exhibit significant dipole components (e.g. Stibbs 1950; Landstreet 1992; Silvester, Kochukhov & Wade 2015).

The origin of the magnetic fields hosted by mCP stars is still unclear (e.g. Moss 2003, 2004); however, it is generally accepted that the observed fields are most likely not being actively generated by dynamo processes such as

those believed to be taking place in the envelopes of cool main sequence (MS) stars (e.g. Charbonneau & MacGregor 2001; Charbonneau 2005; Donati & Landstreet 2009). Arguably, the most plausible explanation is given by the *fossil field* model (Cowling 1945), which states that the fields are slowly-decaying remnants (possibly originating from the interstellar medium or a pre-MS dynamo) from an earlier phase during the star's evolution. This theory is consistent with certain properties of the mCP stars' fields such as their typically simple structures and their long-term stability. The studies carried out by Braithwaite & Nordlund (2006) and Duez & Mathis (2010) also provide important theoretical evidence in support of the fossil field theory: the two studies demonstrate that stable field configurations within the radiative envelopes of upper MS stars – which the fossil field model demands – are a natural consequence of the mag-

netohydrodynamic relaxation of arbitrary initial stochastic fields.

Despite the successes of the fossil field theory, a number of questions regarding the origin of tepid (and hot) star magnetism remain unanswered. For instance, assuming that the fields do originate within the interstellar medium prior to the star’s formation, it is unclear why only a small fraction of MS A-type stars are (strongly) magnetic (e.g. Shorlin et al. 2002; Aurière et al. 2007). Moreover, it is noted that sub-surface convection zones, meridional circulation, and differential rotation are present to varying degrees in early F-, A-, and B-type MS stars. As discussed by Braithwaite & Cantiello (2013), the extent to which these processes may disrupt a fossil field remains an important, unanswered question.

There are also unanswered questions regarding the processes that lead to the horizontal (e.g. Kochukhov et al. 2015; Yakunin et al. 2015; Kochukhov et al. 2017) and vertical (e.g. Babel 1994; Ryabchikova, Wade & Aurière 2005; Rusomarov et al. 2015) chemical abundance stratification in mCP stars. In non-magnetic chemically peculiar (CP) stars, it is believed that sufficiently stable environments (established by slow rotational velocities, suppressed convection, etc.) enable radiation pressure to become dominant thereby allowing specific elements to accumulate within the star’s atmosphere (e.g. Michaud 1970; Michaud et al. 1976; Michaud 1980). The magnetic fields present in the atmosphere’s of mCP stars are also expected to contribute to the environment’s stability; however, it is only relatively recently that magnetic fields have been incorporated into atomic diffusion models (LeBlanc & Monin 2004; Leblanc, Monin & Hauschildt 2009; Alecian & Stift 2010; Alecian 2015). Kochukhov & Ryabchikova (2017) found that the most recent of these theories (Stift & Alecian 2016) cannot reproduce the average surface abundances of Fe-peak elements observed in mCP stars (e.g. Sargent & Searle 1967; Ryabchikova, Leone & Kochukhov 2005; Ryabchikova, Kochukhov & Bagnulo 2008).

The fundamental, chemical, and magnetic properties of mCP stars that have been tested against various models are often inferred from inherently biased surveys: they are either biased towards the brightest objects or those exhibiting the strongest, and thus, most easily detectable magnetic fields. One way in which the influence of observer biases can be reduced is by carrying out a volume-limited survey. Such a survey was initiated by Power (2007), who used the Hipparcos catalogue and the Catalogue of Ap, HgMn and Am stars (Renson, Gerbaldi & Catalano 1991; Renson & Manfroid 2009) to identify a sample of intermediate-mass MS stars within a heliocentric distance of 100 pc. Their work involved the acquisition of a large number of spectropolarimetric Stokes  $V$  measurements using the (now retired) MuSiCoS instrument. These observations allowed for the magnetic parameters of approximately 50% of the mCP stars in the sample to be derived. More recently, we have completed this survey primarily using Stokes  $V$  measurements obtained with ESPaDOnS along with a small number obtained with NARVAL.

Here we present the first results from the volume-limited spectropolarimetric survey of mCP stars located within 100 pc that was initiated in 2007. The goal of this survey is to constrain various fundamental, chemical, and magnetic properties of this stellar population while attempting to min-

imize observational biases. Moreover, since the volume includes a large, effectively complete sample of non-mCP stars with accurate photometric measurements, we can directly compare the magnetic and non-magnetic populations. This provides a unique opportunity to identify the fundamental properties that distinguish the mCP and non-mCP stars. The results presented here will serve as a starting point for the magnetic analysis that will be presented in a subsequent publication, hereinafter referred to as “Paper II”.

In Section 2, we discuss the sample selection including the identification of both confirmed and candidate mCP stars. In Section 3, we briefly summarize the spectropolarimetric observations that were used to (1) confirm whether or not certain candidate mCP stars were magnetic and (2) constrain surface gravities and mean chemical abundances. In Section 4, we assess the completeness of the mCP sample. In Sections 5 and 6, we present the details of the analysis along with our results. Finally, in Section 7, we summarize and discuss the main results from this work.

## 2 SAMPLE SELECTION

### 2.1 Hipparcos Sample

The sample of MS early-F-, A-, and B-type stars was selected from the Hipparcos catalogue (ESA 1997), which consists of 118 218 sources (i.e. single stars, visual multi-star systems, and gravitationally bound multi-star systems) within the solar neighbourhood. It is complete down to magnitudes of  $V = 7.3 - 9.0$  mag depending on the Galactic latitude and spectral type (Perryman et al. 1997). The Tycho catalogue associated with the Hipparcos mission is essentially complete down to magnitudes of  $V \lesssim 9$  mag regardless of sky coordinates. Mignard (2000) estimated the completeness of the Hipparcos sample as a function of Galactic latitude and  $V$  magnitude (Fig. 4 of Mignard 2000) by comparing the number of sources listed in the Hipparcos and Tycho catalogues. These results can be used to assess the level of completeness of our volume-limited sample of MS early-F, A-, and B-type stars taken from the Hipparcos Catalogue by identifying the stars in our sample having faintest  $V$  magnitudes.

The coolest stars in our sample have effective temperatures of  $T_{\text{eff}} \approx 7000$  K with corresponding absolute  $V$  magnitudes of  $M_V \approx 3.2$  mag. At a distance of 100 pc, such stars will have apparent magnitudes of  $V \approx 8.2$  mag. Comparing with Fig. 4 of Mignard (2000), it is apparent that, at  $V = 8.2$  mag, the Hipparcos Catalogue exhibits a minimum completeness of  $\approx 50$  per cent near the Galactic plane. With this in mind, we carried out the following analysis in order to better evaluate the completeness of our sub-sample of MS stars within the Hipparcos Catalogue that are known to have distances  $d < 100$  pc.

Motivated by Mignard (2000), we estimated the completeness of our 100 pc sample by comparing (1) the number of stars in the Hipparcos Catalogue that satisfy our selection criteria (i.e. MS stars with  $T_{\text{eff}} \gtrsim 7$  kK and  $d < 100$  pc) and (2) the number of stars in the Tycho catalogue that either likely or potentially satisfy these criteria. In order to potentially satisfy the criteria, a star in the Tycho catalogue must have  $V < 8.2$  mag,  $T_{\text{eff}} \gtrsim 7$  kK, and a distance that is either known to be  $< 100$  pc or that could be  $< 100$  pc

and exhibit a luminosity greater than that of a zero-age MS star (the minimum  $T_{\text{eff}}$  and minimum luminosity values are based on evolutionary models generated by Ekström et al. (2012) and Mowlavi et al. (2012) and are discussed in more detail in Sect. 5.4). We roughly estimated  $T_{\text{eff}}$  and the bolometric corrections (BCs) for all of the stars in the Hipparcos and Tycho catalogues (ESA 1997) with known  $B$  and  $V$  magnitudes by applying the  $T_{\text{eff}}$  and BC calibrations of Gray (2005) and Balona (1994), respectively. The luminosities for those stars with available parallax (distance) measurements were then derived using the estimated  $T_{\text{eff}}$  and BC values. For the Tycho catalogue stars without available parallax measurements, we assigned  $L(T_{\text{eff}})$  values based on the ZAMS associated with the evolutionary tracks generated by Ekström et al. (2012) and Mowlavi et al. (2012). Adopting this value of  $L(T_{\text{eff}})$  then yields the minimum distance the star could have such that it would remain in our sample after applying the cuts discussed in Sect. 5.4. We find that the estimated completeness of the Hipparcos Catalogue as it pertains to our volume-limited survey of MS stars increases approximately monotonically from 87 per cent at  $T_{\text{eff}} \sim 6.5$  kK to 100 per cent at  $T_{\text{eff}} \sim 19$  kK. A similar trend is found by deriving the masses associated with the estimated  $T_{\text{eff}}$  and  $L$  values (see Sect. 5.4 for a description of the method by which the masses were derived): the completeness increases from  $\sim 87$  per cent for masses of  $M \sim 1.4 M_{\odot}$  to  $\sim 100$  per cent for  $M \gtrsim 3 M_{\odot}$ . We conclude that our results are not likely to be significantly impacted by objects that are missing from the Hipparcos Catalogue (we discuss this in Sect. 6.2 in the context of the incidence rates of mCP stars as a function of mass).

Out of the 118 218 sources in the Hipparcos Catalogue, 23 046 have associated parallax angles – as reported by van Leeuwen (2007) – of  $\pi > 10$  mas corresponding to distances of  $d < 100$  pc. Referring to the Double and Multiple Systems Annex, we find that 5 714 of these sources are either composed of or are members of visual or gravitationally bound multi-star systems; we categorize these systems based on whether or not each of its components have equivalent parallax angles, which are taken from ESA (1997) when no values are reported by van Leeuwen (2007). The subset of 23 046 sources are then found to contain 2 584 (611) astrometrically resolved (unresolved) gravitationally bound multi-star systems. After taking into account the individual components of the resolved systems, a total of 25 720 sources within 100 pc were extracted from the Hipparcos catalogue.

The volume-limited survey presented here is not subject to the Malmquist bias associated with magnitude-limited surveys; however, since the sample selection is based on trigonometric parallax measurements, the sample is affected by the Lutz-Kelker (Trumpler-Weaver) bias (Trumpler & Weaver 1953; Lutz & Kelker 1973). The effect of this bias is to systematically shift the inferred absolute magnitudes for a sample of stars from their true absolute magnitudes. The degree of this shift ( $\Delta M$ ) depends on the sample’s average relative parallax uncertainty,  $\langle \sigma_{\pi}/\pi \rangle$  (Francis 2013, 2014). The 25 720 stars within 100 pc that were extracted from the Hipparcos Catalogue exhibit  $\langle \sigma_{\pi}/\pi \rangle = 0.078$ ; using the quadratic approximation for  $\Delta M$  recommended by Francis (2013), we obtain  $\Delta M = 0.007$  mag. Therefore, the bias is considered to be negligible and no correction was applied.

## 2.2 mCP Subsample

The most definitive method by which all of the mCP stars within 100 pc can be identified is by obtaining costly spectropolarimetric measurements of each early-F-, A-, and B-type MS star. This is unfeasible considering that the sample consists of several thousand such objects. We primarily relied on the Catalogue of Ap, HgMn and Am stars (Renson & Manfroid 2009) in order to identify both candidate and confirmed mCP stars; this allowed us to prioritize specific stars for which new magnetic measurements would be obtained. The catalogue, first compiled by Renson, Gerbaldi & Catalano (1991) and updated several times to include new objects, contains 3 652 stars classified as “definite”, “probable”, or “doubtful” Ap stars, where “Ap” is used broadly to include the magnetic Fp, Ap, Bp, He-weak, and He-strong stars. These classifications are based on whether or not (1) surface magnetic fields have been detected (e.g. Borra & Landstreet 1980; Wade et al. 2000; Bagnulo et al. 2006), (2) characteristic flux abnormalities have been detected based, for instance, on  $\Delta a$  or  $\Delta(V_1 - G)$  photometric colour indices (e.g. Maitzen, Pressberger & Paunzen 1998; Bayer et al. 2000; Paunzen & Maitzen 2005), or (3) chemical peculiarities such as enhanced Si, Cr, or Sr have been reported (e.g. Cowley et al. 1969; Cucchiaro et al. 1978a; Jaschek & Jaschek 1980).

We cross-referenced the list of 25 720 Hipparcos sources with the 3 652 definite Ap (definite mCP), probable Ap (probable mCP), and doubtful Ap (doubtful mCP) stars compiled by Renson & Manfroid (2009) yielding a total of 141 potential mCP stars within 100 pc: 47 of these stars are classified as definite, 27 as probable, and 67 as doubtful mCP stars. We also searched the Catalogue of Stellar Spectral Classifications compiled by Skiff (2014) for stars which had been assigned a ‘p’ classification (e.g. F3p, A0p, etc.) at some point in time. Cross-referencing this catalogue with the 25 720 Hipparcos sources yielded 65 stars not included in the most recently published Catalogue of Ap, HgMn and Am stars. Our tentative list of candidate mCP stars therefore consists of 206 stars.

Using both published magnetic measurements and archived spectropolarimetric data, we conclude that 50 of the 206 stars are magnetic and that 8 are either non-mCP or are weakly-magnetic since no Zeeman signatures were detected (both possibilities suggest that they are not mCP stars). Additionally, no magnetic detections were yielded from measurements of 4 stars obtained by the BinaMICS collaboration (Neiner & Alecian 2013) and of 6 stars obtained by the BRITe-pol collaboration (Neiner et al. 2017) (private communications). No magnetic measurements were available for 138 of the 206 mCP stars and therefore, they could not be confirmed or rejected as mCP members on the basis of magnetic measurements.

The characteristic chemical peculiarities associated with mCP stars can be reliably detected using both UV and optical spectroscopic measurements having relatively low dispersion/resolution (e.g. Cowley 1973; Cucchiaro et al. 1976; Abt 1979). Moreover, mCP stars can be effectively identified using photometric measurements to detect abnormal flux depressions in the UV near 4 100, 5 200, and 6 300 Å (Kodaira 1969; Adelman 1975, 1979). The  $\Delta a$  photometric system introduced by Maitzen (1976) was specifically de-

**Table 1.** List of the 52 confirmed mCP stars and 3 candidate mCP stars within the sample. Columns 1 to 3 list each stars' HD number, identifier (if available), and mCP membership status: confirmed mCP stars are indicated by a 'Y', candidate mCP stars are indicated by a 'U'.

HD	ID	mCP?	HD	ID	mCP?
3980	$\xi$ Phe	Y	112413	$\alpha^2$ CVn	Y
11503	$\gamma^2$ Ari	Y	117025		Y
12447	$\alpha$ Psc A	Y	118022	$\circ$ Vir	Y
15089	$\iota$ Cas	Y	119213	CQ UMa	Y
15144		Y	120198	84 UMa	Y
15717		U	124224	CU Vir	Y
18296	21 Per	Y	128898	$\alpha$ Cir	Y
24712	DO Eri	Y	130559	$\mu$ Lib	Y
27309	56 Tau	Y	137909	$\beta$ CrB	Y
29305	$\alpha$ Dor	Y	137949	33 Lib	Y
32576		U	140160	$\chi$ Ser	Y
38823	V1054 Ori	Y	140728	BP Boo	Y
40312	$\theta$ Aur	Y	148112	$\omega$ Her	Y
49976	V592 Mon	Y	148898	$\omega$ Oph	Y
54118	V386 Car	Y	151199		Y
56022	L01 Pup	Y	152107	52 Her	Y
62140	49 Cam	Y	170000	$\phi$ Dra	Y
64486		Y	176232	10 Aql	Y
65339	53 Cam	Y	187474	V3961 Sgr	Y
72968	3 Hya	Y	188041	V1291 Aql	Y
74067	NY Vel	Y	201601	$\gamma$ Equ	Y
83368		Y	203006	$\theta^1$ Mic	Y
96616	46 Cen	Y	217522	BP Gru	Y
103192	$\beta$ Hya	Y	217831		U
108662	17 Com	Y	220825	$\kappa$ Psc	Y
108945	21 Com	Y	221760	$\iota$ Phe	Y
109026	$\gamma$ Mus	Y	223640	i03 Aqr	Y
112185	$\varepsilon$ UMa	Y			

signed to be sensitive to the 5 200 Å flux depression. A comparable sensitivity to the UV flux depressions can also be obtained from the  $\Delta(V_1 - G)$  and  $Z$  indices derived from filters associated with the Geneva photometric system (Golay 1972; Hauck & North 1982; Cramer 1999).

For the remaining 138 candidate mCP stars, we compiled photometric- and spectroscopic-based evidence of mCP membership from the literature. In a number of cases, stars classified as Fp, Ap, or Bp were done so based solely on abnormally weak individual metal lines (e.g. weak  $\lambda 4481$  Mg II) or were likely misclassified Fm, Am, or  $\lambda$  Bootis stars (e.g. Abt & Morrell 1995a). We used the criteria for detecting CP stars proposed by Paunzen & Maitzen (2005), which are based on  $\Delta a$ ,  $\Delta(V_1 - G)$ , and  $Z$  measurements. The criteria were then applied to the available  $\Delta a$ ,  $\Delta(V_1 - G)$ , and  $Z$  measurements published by Rufener & Nicolet (1988) and Paunzen & Maitzen (2005). In total, 128 stars were found to (1) exhibit photometric measurements consistent with normal or non-mCP stars or (2) were reported to have atmospheric chemical compositions that are not typically associated with mCP stars (e.g. non-peculiar, enhanced Hg and Mn, etc.) and were therefore removed from the list of candidate mCP stars.

Following our derivation of the fundamental parameters (presented in Section 5), we identified three candidate mCP stars in our sample (HD 107452, HD 122811, and HD 177880B) which are likely located beyond the 100 pc

distance limit despite the parallax values reported in the Hipparcos Catalogue. These stars were therefore removed from the sample; this decision is justified in more detail in Section 5.4.

In summary, prior to obtaining new magnetic measurements, we identified 50 definite mCP stars and 7 candidate mCP stars. Only one of the candidate mCP stars, HD 15717, was not found in the catalogue compiled by Renson & Manfroid (2009) and was instead identified using the spectral types compiled by Skiff (2014).

### 3 SPECTROPOLARIMETRIC OBSERVATIONS

Aside from the 7 candidate mCP stars that required magnetic measurements in order to confirm or reject their mCP membership, we also identified a significant fraction of the known mCP stars within the sample for which their magnetic field strengths and geometries could not be sufficiently constrained using previously published and archived magnetic measurements. We therefore proceeded to acquire circularly polarized (Stokes  $V$ ) spectropolarimetric observations in an attempt to overcome these two deficiencies.

The observations were primarily used to detect and measure the stars' longitudinal field strengths; however, the analysis of the fundamental and chemical parameters of the sample that we present here does depend on whether or not we were able to confirm or reject certain candidate mCP stars as being true mCP members. Furthermore, this analysis uses a number of the unpolarized (Stokes  $I$ ) spectra that were acquired with the Stokes  $V$  measurements. Therefore, we briefly summarize the observations here and identify which stars we confirmed as mCP members. The observations are discussed in more detail in Paper II in which we present the magnetic analysis that was performed on the confirmed mCP stars in the sample.

We obtained 118 new Stokes  $V$  observations of 40 mCP and candidate mCP sample stars using the twin spectropolarimeters ESPaDOnS and NARVAL installed at the Canada-France-Hawaii Telescope (CFHT) and the Télescope Bernard Lyot (TBL), respectively. These instruments have a resolving power of  $R \sim 65\,000$  and yield optical spectra within a wavelength range of  $3\,600 \lesssim \lambda \lesssim 10\,000$  Å. Additionally, we analyzed 151 archival Stokes  $V$  observations acquired using the now retired MuSiCoS spectropolarimeter ( $R \sim 35\,000$ ,  $3\,900 \lesssim \lambda \lesssim 8\,700$  Å) that was installed at TBL prior to NARVAL's installation. The MuSiCoS observations were obtained from Feb. 12, 1998 to June 8, 2006.

Based on the new MuSiCoS, ESPaDOnS, and NARVAL Stokes  $V$  measurements, we confirmed that 2 of the candidate mCP stars are magnetic and that 2 are likely not mCP stars since no detections were obtained. In Table 1 we list the 52 confirmed mCP stars located within 100 pc along with the 3 candidate mCP stars which we did not observe.

### 4 DISTRIBUTION AND COMPLETENESS

As discussed in Section 2.1, the Hipparcos Catalogue of early-F-, A-, and B-type MS stars can reliably be considered to be complete within 100 pc; however, the complete-

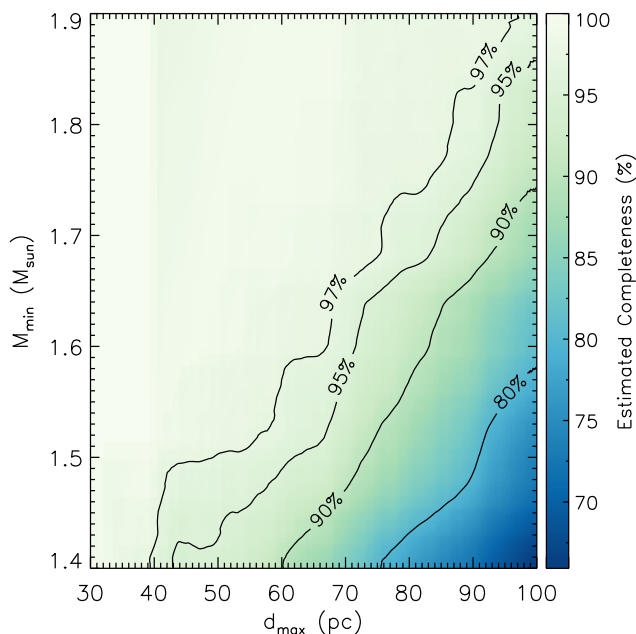


**Figure 1.** Estimated completeness of the mCP subsample within 100 pc. The values are based on the fraction of the sample’s early-F-, A-, and B-type MS stars for which suitable photometric or spectroscopic measurements have been obtained (i.e. those capable of distinguishing between mCP and non-mCP stars).  $d_{\max}$  and  $M_{\min}$  correspond to the adopted distance limit and the minimum stellar mass of the sample. The fraction decreases for larger volumes (greater distance limits) and for lower masses as a result of an increasing sample size.

ness of the subsample of mCP stars needs to be assessed. Magnetic measurements, which provide the most conclusive evidence of mCP membership, have not been obtained for the vast majority of the larger sample of Hipparcos stars. On the other hand, spectroscopic and photometric measurements, some of which can be used to distinguish between mCP stars and non-mCP stars, are available for many of the stars in the sample. We estimated the completeness of the mCP subsample by determining the fraction of the total sample for which such mCP-sensitive measurements have been reported in the literature. Note that the following estimates correspond to the sample of early-F-, A-, and B-type MS stars having masses  $> 1.4 M_{\odot}$  (derived in Section 5.4), which consists of 3254 stars.

Paunzen & Maitzen (2005) found that mCP stars can be identified with an efficiency of  $\approx 91$  per cent based on  $\Delta a$  measurements and  $\approx 83$  per cent based on  $\Delta(V_1 - G)$  measurements. Using the published catalogues, we find that 9 per cent of the sample’s 3254 stars have available  $\Delta a$  measurements (Maitzen, Pressberger & Paunzen 1998; Vogt et al. 1998; Paunzen & Maitzen 2005) while 46 per cent have available Geneva measurements (Rufener & Nicolet 1988). Eighty-four per cent of the sample stars have spectral classifications listed in the Catalogue of Stellar Spectral Classifications (Skiff 2014); however, many of the spectroscopic measurements used to derive these classifications may be insensitive to chemical peculiarities due to insufficient resolution. For those classifications derived from optical spectra, we only considered those measurements obtained with dis-

persions  $> 90 \text{ \AA mm}^{-1}$  (Young & Martin 1973; Abt 1979) or resolutions  $< 3 \text{ \AA}$ . Those classifications derived from the UV spectra obtained using the S2/68 instrument onboard the TD1 satellite were also considered reliable despite the low resolution of  $\approx 37 \text{ \AA}$  (Wilson et al. 1972). This is based on the fact that, similar to the  $\Delta a$  and  $\Delta(V_1 - G)$  photometric measurements, the S2/68 measurements are sensitive to UV flux depressions characteristic of many mCP stars (Cucchiari et al. 1976, 1977, 1978a,b, 1980).

The strength of the photometric peculiarity indices induced by the presence of strong surface magnetic fields is known to decrease with decreasing  $T_{\text{eff}}$  (Maitzen 1976; Maitzen, Weiss & Wood 1980; Maitzen & Vogt 1983; Masana et al. 1998). Moreover, as  $T_{\text{eff}}$  decreases, a greater number of mCP stars is found to exhibit non-peculiar  $\Delta a$  and  $\Delta(V_1 - G)$  values (e.g. Fig. 4 of Maitzen 1976). We find that our full sample contains 9 stars classified as non-mCP based solely on  $\Delta a$  measurements and 299 based solely on  $\Delta(V_1 - G)$  measurements. We estimated the fraction of these 308 stars that may actually be undetected mCP stars by referring to Table 5 of Paunzen & Maitzen (2005): the authors find that 1.4 per cent and 2.2 per cent of their sample’s mCP stars exhibit non-peculiar  $\Delta a$  and  $\Delta(V_1 - G)$  measurements, respectively. Therefore, we estimate that our sample contains no additional undetected mCP stars based on  $\Delta a$  based classifications (i.e.  $9 \times 0.014 < 1$ ) and 6 additional undetected mCP stars based on  $\Delta(V_1 - G)$  based classifications (i.e.  $299 \times 0.022 < 7$ ). Although we cannot provide precise constraints on the most-probable temperatures of these stars, it is likely that they are cooler stars with  $T_{\text{eff}} \lesssim 7 \text{ kK}$  based on the fact that a greater number of mCP stars are found to exhibit peculiarity indices that are largely indistinguishable from non-mCP stars at lower temperatures (e.g. Maitzen 1976).

Considering the total sample, we find that 1924 of the 3254 stars (67 per cent) have been observed using spectroscopic and photometric methods capable of distinguishing between mCP and non-mCP stars. However, this number changes significantly based on the adopted lower mass limit ( $M_{\min}$ ) and the adopted distance limit ( $d_{\max}$ ) associated with the sample; in Fig. 1, we show the estimated completeness as a function of  $d_{\max}$  and  $M_{\min}$ . Evidently, the 100 pc sample of confirmed and candidate mCP stars has a completeness of  $\approx 90$  per cent for masses  $\gtrsim 1.7 M_{\odot}$ . This completeness is more representative of the sample compared to the 67 per cent value derived using  $M_{\min} = 1.4 M_{\odot}$  given that 91 per cent of the sample of confirmed and candidate mCP stars have masses  $\gtrsim 1.7 M_{\odot}$ .

We also performed two basic tests to look for obvious indications that the sample of mCP stars is incomplete. Both of the tests are based on the assumption that the spatial distribution of these particular objects within the sample’s 100 pc distance limit is approximately random and uniform. Under this assumption, we would expect nearly the same number of mCP stars to be located in both the northern and southern hemispheres. In Fig. 2, we plot the sky coordinates of the confirmed mCP stars, candidate mCP stars, and the non-mCP stars using an equal-area Hammer-Aitoff projection. Considering the 52 confirmed mCP stars in the sample, we find a ratio of the number of northern stars ( $N_N$ ) to southern stars ( $N_S$ ) of 1.08; including the 3 candidate mCP stars yields  $N_N/N_S = 1.08$  as well. The signif-

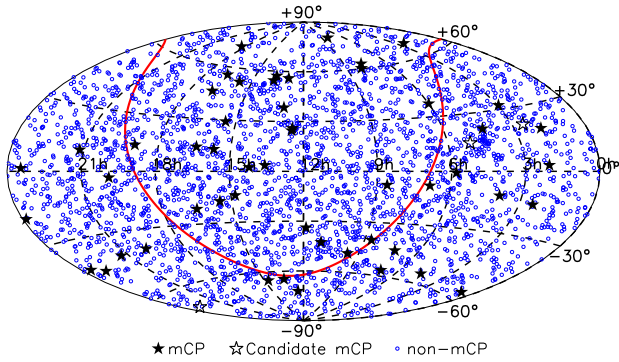


**Figure 2.** Equatorial coordinates of the mCP stars (black, filled stars), candidate mCP stars (black, open stars) and non-mCP stars (blue circles). The solid red curve corresponds to the Galactic plane.

ificance of these ratios can be assessed using a Monte Carlo (MC) simulation. We generated  $10^5$  distributions containing 52 and 55 randomly assigned latitude values according to  $\theta = \pi/2 - \cos^{-1}(2x - 1)$ , where  $x$  is a uniformly distributed random number between 0 and 1 (e.g. Kochukhov & Sudnik 2013). The simulated  $N_N/N_S$  distributions suggest that the values derived from the subsample of 52 confirmed mCP stars and the combined subsample of 52 confirmed and 3 candidate mCP stars are consistent with random distributions at 68 per cent and 79 per cent confidence levels, respectively.

The second test simply involves comparing the distribution of the mCP subsample’s distances to that of a spatially uniform distribution. This is shown in Fig. 3 in which the cumulative distribution function (CDF) of the distances to the mCP stars is plotted along side that expected from a sample with a uniform spatial distribution. Although the sample of confirmed and candidate mCP stars exhibits a slight excess between 50 and 70 pc, the Kolmogorov-Smirnov (KS) test statistic implies that the distance distribution is consistent with that of a uniform distribution: we calculated a KS statistic of  $0.13 \pm 0.13$  where the uncertainty corresponds to  $3\sigma$  (the uncertainty was derived using the bootstrapping method of case resampling in which the KS statistic was calculated for 1000 distance distributions generated by randomly sampling the empirical distance distribution).

## 5 DERIVATION OF FUNDAMENTAL PARAMETERS

Several techniques were employed in order to derive fundamental parameters (effective temperature, surface gravity, mass, radius, and age) for all of the stars in the sample. For the non-mCP stars and 3 candidate mCP stars in the survey, we used various photometric calibrations depending on the available archival measurements. A more detailed analysis of both photometric and spectroscopic measurements was carried out for the 52 confirmed mCP stars.

Archival broad-band photometric measurements were obtained from the General Catalogue of Photometric Data (Mermilliod, Mermilliod & Hauck 1997). The catalogue consists of measurements of over 200 000 stars that were obtained using a wide range of photometric systems. In addi-

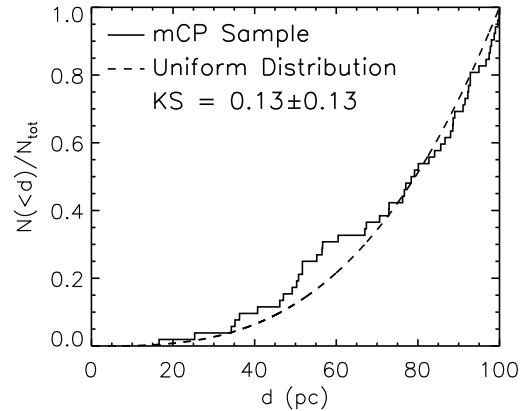


**Figure 3.** Cumulative distribution function of the mCP star distances (solid black) normalized to the total number of mCP stars. The dashed black curve corresponds to the CDF associated with a spatially uniform distribution. Comparing the two distributions yields a Kolmogorov-Smirnov test statistic of  $0.13 \pm 0.13$ .

tion to the Johnson  $V$ , Hipparcos  $H_p$ , and Tycho  $V_T$  and  $B_T$  observations (ESA 1997), we also used observations obtained with Geneva  $UB_1BB_2V_1VG$  filters (Rufener & Nicolet 1988), Johnson  $UVBRI$  filters (Hoffleit & Jaschek 1991; Ducati 2002), Strömgren  $uvby$  filters (Hauck & Mermilliod 1997), and 2MASS  $JHK_s$  filters (Cohen, Wheaton & Megeath 2003). In some cases, no uncertainties for these observations were reported and we adopted values of 1 per cent. Since the sample is limited to stars with  $d < 100$  pc, we assumed that – for both the mCP and non-mCP stars – photometric reddening caused by interstellar extinction is negligible ( $E[b - y] \lesssim 0.02$ , Vergely et al. 1998).

### 5.1 non-mCP subsample

We used three photometric temperature calibrations defined within the Johnson, Geneva, and Strömgren systems in order to derive  $T_{\text{eff}}$  for the non-mCP stars. The calibrations published by Gray (2005) were applied to the available Johnson  $B$  and  $V$  filter measurements that are appropriate for both “cool” MS stars ( $T_{\text{eff}} \lesssim 10^4$  K or  $B - V > 0.0$ , Eqn. 14.17) and “hot” MS stars ( $T_{\text{eff}} \gtrsim 10^4$  K or  $B - V < 0.0$ , Eqn. 14.16). For those stars for which measurements obtained using the Geneva system are available, we applied the calibrations of Künzli et al. (1997), which are suitable for MS stars with  $T_{\text{eff}} \gtrsim 5000$  K. Lastly, for those cases in which measurements obtained using the Strömgren system are available, we applied the calibrations of Balona (1994), which are suitable for MS stars with  $5500 \text{ K} < T_{\text{eff}} < 35000 \text{ K}$ .

In Fig. 4 we compare  $T_{\text{eff}}$  derived using the three calibrations (for those stars for which more than one calibration could be applied). In general, we find reasonable agreement between the calibrations for  $T_{\text{eff}} \lesssim 10^4$  K. At higher temperatures, both the calibrations involving Geneva filters ( $T_{\text{eff}}^{\text{Geneva}}$ ) and Strömgren filters ( $T_{\text{eff}}^{\text{Strömgren}}$ ) tend to predict higher  $T_{\text{eff}}$  values compared to those involving Johnson  $B$  and  $V$  filters ( $T_{\text{eff}}^{\text{Johnson}}$ ). In Fig. 4 (top right) we show the distribution of  $T_{\text{eff}}^{\text{Johnson}}$  derived for those stars that only have Johnson  $B$  and  $V$  measurements available (i.e. no  $T_{\text{eff}}^{\text{Geneva}}$  or  $T_{\text{eff}}^{\text{Strömgren}}$  values could be derived). It is evident that the majority of the non-mCP stars in the sample ( $\approx 62$  per cent)

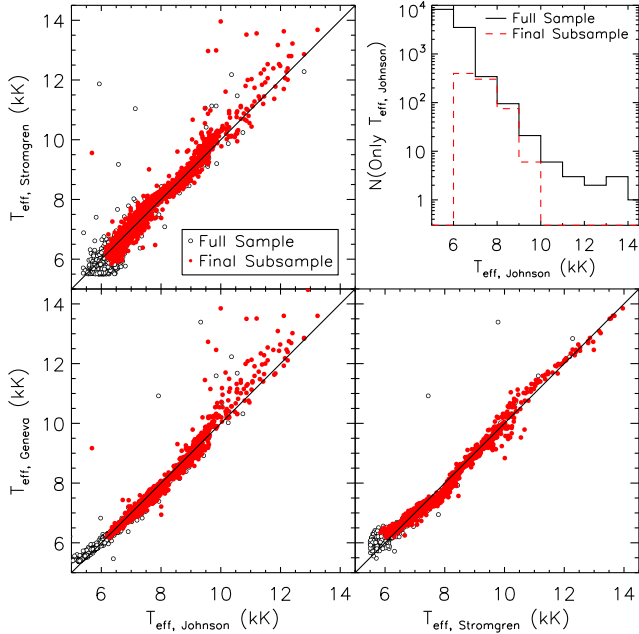


**Figure 4.** *Top left and bottom row:* Comparison between the  $T_{\text{eff}}$  values of the non-mCP stars derived using three calibrations: Künzli et al. (1997) (Geneva filters), Balona (1994) (Strömgren filters), and Gray (2005) (Johnson filters). The open black circles correspond to the full sample of non-mCP stars extracted from the Hipparcos Catalogue; the filled red circles correspond to the subsample remaining after applying several cuts to the full sample (described in Sect. 5.4). *Top right:* Distribution of non-mCP stars in the sample for which only Johnson photometric measurements are available.

fall into this category; however, only 24 of those stars exhibit  $T_{\text{eff}} > 10^4$  K (i.e. the maximum temperature at which  $T_{\text{eff}}^{\text{Johnson}}$  may be considered reliable). We note that, after applying several cuts to the total sample as described in Sect. 5.4, all of the hotter stars without available Geneva or Strömgren photometry were removed.

When more than one calibration was applied, the final effective temperatures of each non-mCP star were taken to be the average of these values. If  $T_{\text{eff}}^{\text{Johnson}}$  was found to differ significantly from  $T_{\text{eff}}^{\text{Geneva}}$  and/or  $T_{\text{eff}}^{\text{Strömgren}}$ , we removed  $T_{\text{eff}}^{\text{Johnson}}$  prior to averaging. A uniform uncertainty of 5 per cent was adopted for each of the final  $T_{\text{eff}}$  values based on the dispersion in the  $T_{\text{eff}}^{\text{Johnson}} - T_{\text{eff}}^{\text{Geneva}}$  and  $T_{\text{eff}}^{\text{Johnson}} - T_{\text{eff}}^{\text{Strömgren}}$  planes shown in Fig. 4.

The luminosity ( $L$ ) of each of the non-mCP stars was derived by first applying the bolometric correction (BC)- $T_{\text{eff}}$  relation published by Balona (1994), which is applicable to MS stars with  $T_{\text{eff}} \gtrsim 5500$  K. The absolute magnitude ( $M_V$ ) values derived from the Hipparcos  $V$  and  $\pi$  measurements (ESA 1997; van Leeuwen 2007) were then used in conjunction with the BC values to calculate each star’s absolute bolometric magnitude ( $M_{\text{bol}}$ ), and thus, their luminosities (we used a solar absolute bolometric magnitude of 4.74 for this calculation). The stellar radii ( $R$ ) were derived using the Stefan-Boltzmann relation with each star’s  $T_{\text{eff}}$  and  $L$ . As with  $T_{\text{eff}}$ , we adopted a uniform 5 per cent uncertainty in  $L$ ; the uncertainty in  $R$  was derived by propagating the uniform  $T_{\text{eff}}$  and  $L$  uncertainties.

## 5.2 mCP subsample

Various photometric temperature calibrations that are applicable to mCP stars are available in the literature. (e.g. Hauck & North 1993; Stepień 1994). However, unlike for the non-mCP stars, we have high-resolution spectra available for nearly all of the mCP stars in this sample. We therefore opted to derive each mCP star’s fundamental parameters by employing a more detailed method of iteratively fitting (1) the photometry to synthetic spectral energy distributions (SEDs) and (2) the observed spectra to model spectra (a similar method is described by Silvester, Kochukhov & Wade 2015). In this approach, we generated model atmospheres and their associated SEDs that took into account chemical peculiarities and strong surface magnetic fields. Chemical peculiarities and, to a lesser extent, surface magnetic fields can significantly modify a star’s SED by redistributing flux from UV to redder wavelengths (Kodaira 1969; Stepień 1978; Kupka, Pauzen & Maitzen 2003); therefore, it is often important to take these effects into account when deriving fundamental parameters by fitting SEDs.

Our analysis consisted of three iterations which we outline now and describe more thoroughly in the following subsections. In the first iteration, we obtained an estimate of  $T_{\text{eff}}$  and radius ( $R$ ) by fitting the photometric observations to a grid of synthetic SEDs. Individual metallic spectral lines (e.g. Cr, Fe, Mg) were then isolated from various spectroscopic observations. These measurements were fit to models in order to derive the projected rotational velocity ( $v \sin i$ ). Next, we estimated  $\log g$  by fitting the available H $\beta$  and H $\gamma$  observations. Finally, wide spectral regions containing a large number of He and metallic lines (i.e. no Balmer lines) were fit in order to derive estimates of the chemical abundances.

The first iteration yielded estimates of  $T_{\text{eff}}$ ,  $\log g$ , and the chemical abundances. For the second iteration, these parameters were used to generate a small grid of atmospheric models and synthetic SEDs, which took into account the effects of chemical peculiarities and strong magnetic fields (the magnetic field strengths are derived in Paper II). The grid consisted of models spanning a narrow range of  $T_{\text{eff}}$ . The photometric measurements were then refit using this new grid, which yielded more refined values of both  $T_{\text{eff}}$  and  $R$ . With a new value of  $T_{\text{eff}}$  derived, the observed spectra were once again fit in order to refine  $\log g$  and the chemical abundances.

The third and last iteration simply involved recalculating single atmospheric models and synthetic SEDs using the final values of  $T_{\text{eff}}$ ,  $\log g$ , the chemical abundances, and the magnetic field strength (if a sufficiently strong magnetic field was inferred). A final value of  $R$  was then derived by fitting the photometry to the synthetic SED.

### 5.2.1 SED fitting

In order to fit the observed photometric measurements, we first generated a grid of model atmospheres with accompanying synthetic SEDs spanning a range of  $T_{\text{eff}}$  and  $\log g$ . We used the LLMODELS code, which calculates plane-parallel model atmospheres under the local thermodynamic equilibrium (LTE) assumption (Shulyak et al. 2004). This code is well-suited to this study primarily because it allows for

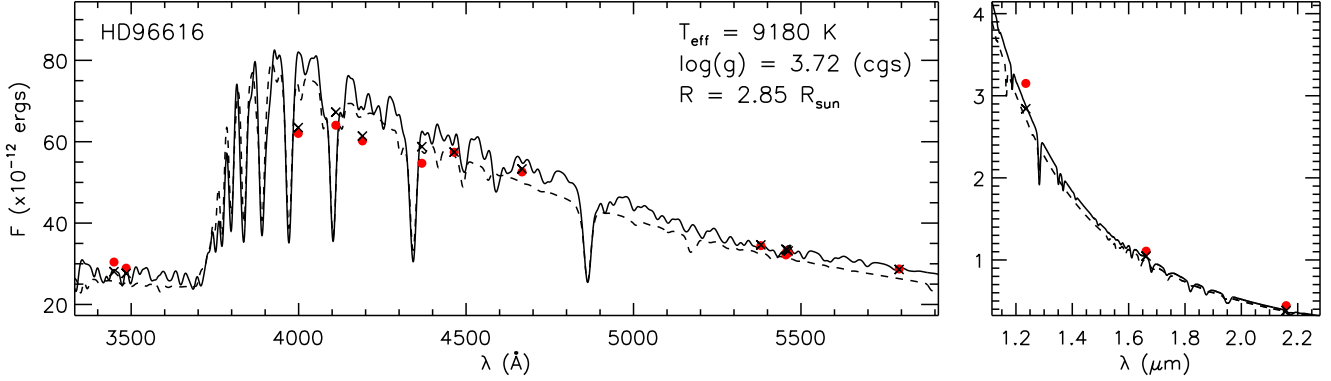


**Figure 5.** An example of the final fit to the observed photometry (filled circles) of HD 96616. The left panel shows the optical photometry (Johnson, Geneva, and Strömgren) while the right panel shows the 2MASS photometry. The solid black line is the detailed synthetic SED while the black ‘X’ symbols correspond to the synthetic flux of each photometric filter used in the comparisons with the observations. The dashed black line shows the solar metallicity synthetic SED calculated without taking into account chemical peculiarities or magnetic fields. Both of the synthetic SEDs have been convolved with a Gaussian function consistent with  $v \sin i = 1000 \text{ km s}^{-1}$  for visual clarity.

abundances of individual elements to be varied rather than simply scaling all abundances with  $[M/H]$ . Furthermore, it can also include the anomalous Zeeman effect induced by the presence of strong surface magnetic fields (Kochukhov, Khan & Shulyak 2005).

For the first iteration, the grid of model atmospheres and synthetic SEDs was calculated for  $5500 \text{ K} \leq T_{\text{eff}} \leq 10000 \text{ K}$  in increments of 100 K and for  $10000 \text{ K} \leq T_{\text{eff}} \leq 20000 \text{ K}$  in increments of 250 K. We used a solar metallicity ( $[M/H] = 0.0$ ), which is based on the solar abundances reported by Asplund et al. (2009). Both the microturbulence ( $v_{\text{mic}}$ ) and the surface gravity were fixed at  $0 \text{ km s}^{-1}$  and 4.0 (cgs), respectively, while all other physical parameters were unmodified from their default values.

The output flux associated with the synthetic SEDs – given in physical flux units of  $\text{erg/s/cm}^2/\text{\AA}$  – was used to calculate the flux associated with various photometric filters. Transmission functions for the relevant filters – Hipparcos, Johnson, Tycho (Bessell & Murphy 2012), Geneva (Rufener & Nicolet 1988), Strömgren (Bessell 2011), and 2MASS (Cohen, Wheaton & Megeath 2003) – were obtained from the literature. These functions were then normalized, interpolated to the wavelength abscissa of each synthetic SED using a spline method, and multiplied by the associated flux. The resulting curves were then integrated yielding the total stellar flux contributed to each filter.

We converted the observed magnitudes of each star to physical flux units using zero point values reported in the same publications that the filter transmission functions were obtained from. The best-fitting model SED associated with the observed flux values was then derived using a Levenberg-Marquardt algorithm (LMA) implemented in IDL with 2 free parameters:  $T_{\text{eff}}$  and the scaling factor  $\alpha \equiv (R/d)^2$ . The free parameters were allowed to vary continuously, which required an interpolation (we used a spline interpolation method) of the model grid in  $T_{\text{eff}}$ .

A similar SED fitting procedure was applied during the second iteration using a narrower grid of synthetic SEDs. This grid consisted of between 4 and 6 models bracketing the current value of  $T_{\text{eff}}$  in increments of 500 K and included the derived chemical abundances (discussed in Section 5.2.3)

and magnetic fields (if the field strength derived in Paper II was found to exceed 5 kG). For those elements whose abundances were not derived, we used the values associated with a solar metallicity. The final value of the scaling factor  $\alpha = (R/d)^2$  was used to derive  $R$ ; the final values of  $T_{\text{eff}}$  and  $\alpha$  were used in conjunction with the Stefan-Boltzmann relation to derive each star’s luminosity:

$$\frac{L}{L_{\odot}} = \alpha \frac{d^2}{R_{\odot}^2} \left( \frac{T_{\text{eff}}}{T_{\text{eff},\odot}} \right)^4 = \left( \frac{R}{R_{\odot}} \right)^2 \left( \frac{T_{\text{eff}}}{T_{\text{eff},\odot}} \right)^4. \quad (1)$$

The uncertainties in  $T_{\text{eff}}$  and  $\alpha$  were estimated through the method of residual bootstrapping. In this procedure, the residuals associated with the best-fitting synthetic SED are first scaled using each data point’s estimated statistical leverage and subsequently centered by subtracting the mean residual (Davison & Hinkley 1997). A distribution of 1000 data sets was then generated by randomly sampling the scaled and centered residuals and adding them to the fitted flux values. Distributions of  $T_{\text{eff}}$  and  $\alpha$  were then obtained by fitting synthetic SEDs to the 1000 bootstrapped data sets thereby allowing  $3 \sigma$  uncertainties to be estimated from the distribution widths. Since the luminosity is expected to be correlated (to some extent) with both  $T_{\text{eff}}$  and  $\alpha$ , we estimated the uncertainty in  $\log L$  using the bootstrapped distributions of  $T_{\text{eff}}$  and  $\alpha$ . Lastly, the reported uncertainties in the Hipparcos parallaxes (van Leeuwen 2007) were factored into the uncertainties in  $R$  and  $\log L$  using a standard error propagation method.

An example of the final fit to the photometry that was obtained after two iterations of chemical abundance and  $\log g$  derivations is shown in Fig. 5.

### 5.2.2 Balmer line fitting

The shape of the broad Lorentzian wings of the Balmer lines is relatively sensitive to variations in the surface gravity, particularly for  $T_{\text{eff}} \gtrsim 10000 \text{ K}$  (we found that the sensitivity tends to decrease with decreasing  $T_{\text{eff}}$ ). We derived  $\log g$  by fitting  $H\beta$  and  $H\gamma$  profiles. This analysis depends crucially on the normalization that is applied to these measurements; therefore, measurements obtained using certain

instruments for which automatic normalization was carried out by the reduction pipeline (e.g. MuSiCoS) could not be used for this purpose. We used NARVAL and ESPaDOnS spectra – both new and archival observations – along with archived ELODIE, HARPS, SOPHIE, and UVES spectra.

The spectral orders extracted from cross-dispersed échelle spectra – such as ESPaDOnS and NARVAL – are known to exhibit an intrinsic curvature. This can yield biased results when modelling the broad wings of the Balmer lines, particularly for those that are incident near the edges of the extracted orders (e.g.  $H\beta$  in ESPaDOnS and NARVAL spectra). For the A- and B-type stars composing our survey, the extracted orders exhibit continua that are approximately linear near  $H\gamma$  and  $H\beta$ ; therefore, fits to  $H\gamma$  and  $H\beta$  profiles that have been normalized using a local linear fit (described below) should be relatively unaffected by the intrinsic curvature. In Fig. 6, a number of examples of the final fits to  $H\gamma$  and  $H\beta$  lines are shown where, in some cases, relatively small discrepancies between the model and the observed spectra are apparent within the wings. This may be evidence that some of the ESPaDOnS and NARVAL spectra are noticeably affected by distortions in the continuum or normalization discrepancies. It is noted that any systematic error in  $\log g$  introduced by this aspect of the observed spectra is likely less than the uncertainty introduced by the degeneracy between  $T_{\text{eff}}$  and  $\log g$  (the estimation of  $\log g$  uncertainties is discussed at the end of this section).

For each measurement, we first derived radial velocities by fitting a Gaussian function to the Doppler core of  $H\beta$  and  $H\gamma$ ; the wavelengths of the spectra were then adjusted to remove these radial velocities. Next, each of the Balmer line profiles were individually normalized by applying a linear fit to narrow continuum regions located on either side of the line’s core at  $\approx \pm 35 \text{ \AA}$  relative to the central wavelength ( $\lambda_0$ ). Lastly, the normalized measurements of each star’s  $H\beta$  and  $H\gamma$  profiles were grouped into sets based on the instrument with which they were obtained. The measurements within each of these sets were then interpolated onto a common wavelength abscissa – ranging from  $-40$  to  $+40 \text{ \AA}$  relative to  $\lambda_0$  – and the associated flux values were averaged. Care was taken to ensure that, prior to averaging, the flux values near the continuum regions at  $\lambda_0 \pm 35 \text{ \AA}$  were approximately equal.

We fit the averaged  $H\beta$  and  $H\gamma$  profiles using the Grid Search in Stellar Parameters (GSSP) code developed by Tkachenko (2015). This code uses atmospheric models provided by LLMODELS and chemical line lists provided by the Vienna Atomic Line Database (VALD) (Piskunov et al. 1995; Kupka et al. 2000) to generate model spectra associated with a set of input parameters (e.g.  $T_{\text{eff}}$ ,  $\log g$ ,  $v \sin i$ ,  $v_{\text{mic}}$ , and individual atmospheric chemical abundances) under the LTE assumption. GSSP differs from similar spectral line fitting codes (e.g. SME, Valenti & Piskunov 1996) in that it generates grids of models corresponding to the range and increments of the specified input parameters and compares  $\chi^2$  values in order to determine the best-fitting model.

The method used by GSSP is computationally expensive since a large number of models are typically produced. We reduced the total computation time by first roughly estimating  $\log g$  by eye, then allowing the chemical abundances to be fit individually to within 1.0 dex. The abundances were then fixed and GSSP was used to determine the best-fitting value

of  $\log g$  to within 0.1 (cgs). The specific elements that were included in each fit were selected by referring to a VALD line list generated using an Extract Stellar request with the current estimate of  $T_{\text{eff}}$  and  $\log g$ ; all elements exhibiting lines within the wavelength region to be fit having normalized depths  $\geq 0.1$  were then identified and their abundances were allowed to vary. The second iteration was carried out in a similar fashion; however, narrower abundance and  $\log g$  grids were adopted having increments of 0.1 dex and 0.01 (cgs), respectively. Instrumental broadening was included in the model calculations by specifying the resolving power of the instrument used to obtain the observation. The microturbulence was fixed at  $0 \text{ km s}^{-1}$  throughout the analysis while  $v \sin i$  was fixed at the values derived during the first iteration of He and metallic line fitting (see Section 5.2.3). Several examples of the final fits to the  $H\beta$  and  $H\gamma$  lines are shown in Fig. 6 for a range of  $v \sin i$  values.

We typically found small discrepancies between the values of  $\log g$  derived from the modelling of each star’s  $H\gamma$  and  $H\beta$  measurement. These discrepancies provide an estimate of the uncertainty in  $\log g$  resulting from statistical noise and continuum normalization inaccuracies. By far, the largest contribution to the uncertainty in  $\log g$  results from the slight degeneracy between  $\log g$  and  $T_{\text{eff}}$ : similar-quality fits to the Balmer lines can be derived using a range of  $\log g$  and  $T_{\text{eff}}$  values. We derived uncertainties in  $\log g$  by carrying out the fitting routine using both the minimal and maximal values of  $T_{\text{eff}}$  associated  $\sigma_{T_{\text{eff}}}$ . The derived  $\log g$  values are listed in Table 2.

### 5.2.3 He and metallic line fitting

Spectroscopic measurements obtained by various instruments – including those which could not be used for the Balmer line fitting analysis – were used to derive each mCP star’s chemical abundances and  $v \sin i$  values. As in Section 5.2.2, we opted to perform this analysis on averaged spectra obtained by combining multiple measurements. This was carried out by first calculating and subsequently removing the radial velocity shift of each measurement. The radial velocities were derived by fitting a Gaussian function to the Doppler cores of several Balmer lines ( $H\alpha$ ,  $H\beta$ , and  $H\gamma$  depending on the wavelength span of the spectra) and averaging the results.

We selected nine spectral regions to be fit from 5000 to 5900  $\text{\AA}$ , each 100  $\text{\AA}$  in width. These regions were selected primarily because of (1) the absence of Balmer lines and (2) the reasonably (but not excessively) high density of metallic lines; lower wavelength regions (e.g.  $\lambda \sim 4000 \text{ \AA}$ ) exhibit a higher density of both Balmer and metallic lines, which tend to increase the number of blended lines and introduce systematic errors associated with the normalization procedure. The selected regions were individually normalized by fitting a multi-order polynomial to the continuum. Each set of spectra covering these regions that were obtained using the same instruments were then compared in order to ensure consistent normalization. They were then interpolated onto a common wavelength abscissa and averaged. The normalized average spectra were subdivided into smaller regions having widths of 25 or 50  $\text{\AA}$  depending on the number of lines found in each of the 100  $\text{\AA}$  spectral regions: observations from stars having sharp lines, such as HD 217522

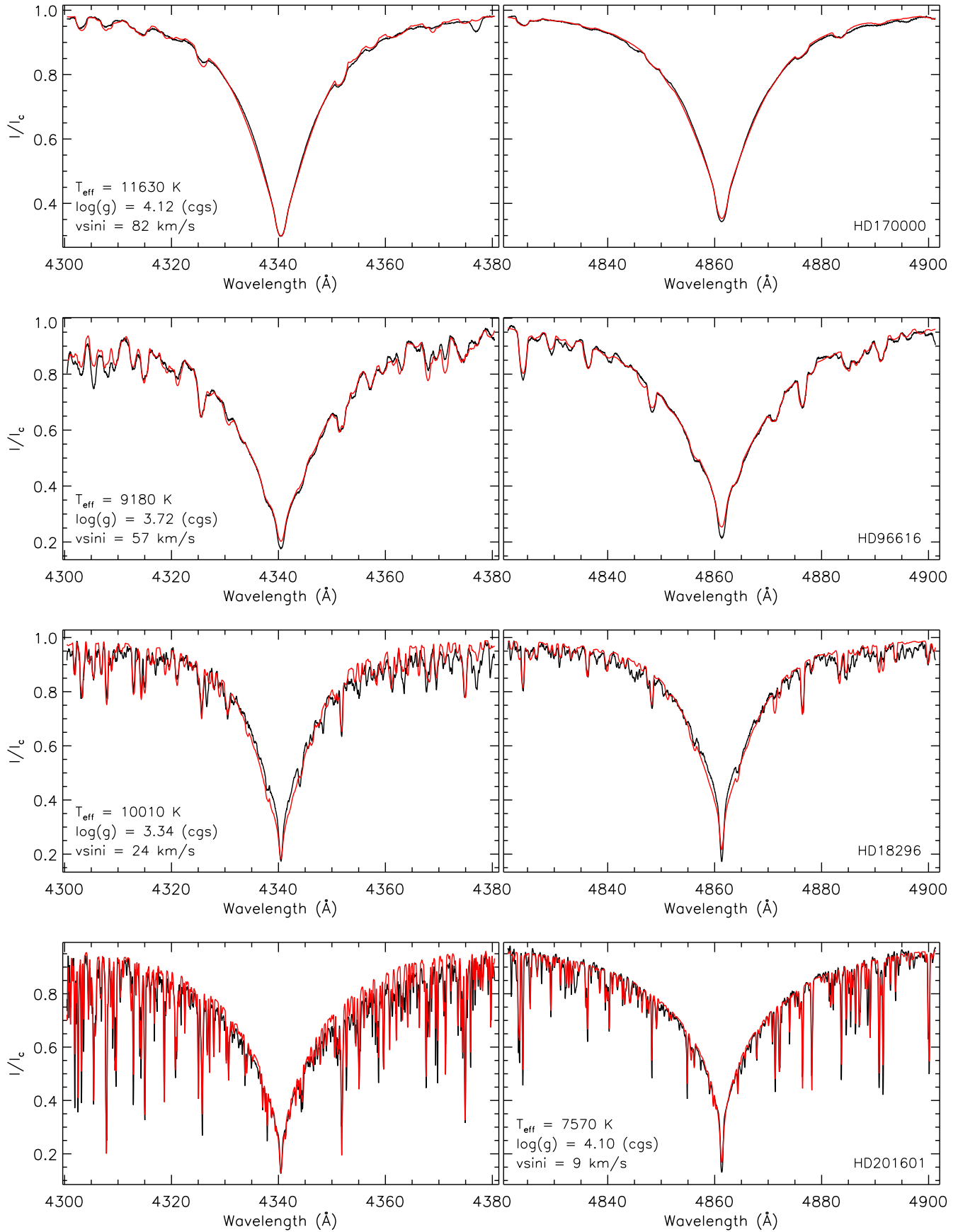


**Figure 6.** Examples of the final fits to the observed H $\gamma$  (left) and H $\beta$  (right) profiles. The black curves correspond to the averaged observed spectra while the red curves are the best-fitting models calculated using GSSP.

( $v \sin i \approx 5 \text{ km s}^{-1}$ ) were subdivided into 25 Å regions while those exhibiting exceptionally broad lines such as HD 124224 ( $v \sin i \approx 150 \text{ km s}^{-1}$ ) were either subdivided into 50 Å regions or left as 100 Å regions.

We proceeded to fit these 25 to 100 Å width spectral regions using an optimized version of the ZEEMAN spectrum synthesis code, which solves the polarized radiative transfer equations under the LTE assumption (Landstreet 1988; Wade et al. 2001a). These fits were initially carried out without including the effects of magnetic fields (see discussion below). The optimizations were implemented by Folsom et al. (2012), who also developed a Levenberg-Marquardt algorithm (LMA) to be used in conjunction with ZEEMAN in order to determine a minimal  $\chi^2$  solution for a given set of free parameters ( $T_{\text{eff}}$ ,  $\log g$ ,  $v \sin i$ , etc.). The relevant data for each spectral line (i.e. wavelength, depth, excitation energy, etc.) were obtained from VALD3 (Ryabchikova et al. 2015) using an Extract Stellar request for a range of  $T_{\text{eff}}$  values from 6000 to 20000 K, a detection threshold of 0.005, and  $\log g = 4.0$  (cgs).

We first used the ZEEMAN LMA to derive the  $v \sin i$  value associated with individual (non-averaged) spectra of each star. This was done by isolating a large number of individual metallic lines, which appeared to be unblended, and applying the fitting routine;  $T_{\text{eff}}$  was fixed at the value derived from the first iteration’s fit to the photometry,  $\log g$  and  $v_{\text{mic}}$  were fixed at 4.0 (cgs) and  $0 \text{ km s}^{-1}$ , respectively, while the abundance associated with the identified line and the value of  $v \sin i$  were allowed to vary. Any resulting fits to these lines that were judged by eye to be inadequate – likely as a result of systematic errors associated with non-uniform surface abundance distributions (e.g. Kochukhov et al. 2004) – were removed from the analysis. The value and uncertainty of  $v \sin i$  were then derived by taking the median and mean absolute deviation of the  $v \sin i$  values associated with the accepted fits, which ranged in number from 7 to 85 per star.

Depending in part on the strength of each star’s magnetic field and the value of  $v \sin i$ , Zeeman broadening may have a non-negligible contribution to the width and overall profile of a given spectral line. Therefore, we repeated the  $v \sin i$  derivation with the inclusion of a dipole surface magnetic field. The strength of the field ( $B_d$ ), obliquity angle ( $\beta$ ), and inclination angle of the axis of rotation ( $i$ ) were estimated using the method described in Paper II. These three parameters could not be derived for five stars due to an insufficient number of obtained observations and/or because of exceptionally long rotational periods, which generally prevents  $v \sin i$  (and thus,  $i$ ) from being accurately constrained. In these cases, we adopted  $B_d$  values estimated using Eqn. 6 of Aurière et al. (2007) and  $i = \beta = 45^\circ$ .

For those stars for which both  $v \sin i$  values (i.e. the values derived with and without including Zeeman broadening) were found to be in agreement, we adopted the value exhibiting a lower uncertainty. Similarly, if more precise published values that are also in agreement with our derived values are available, we adopted the published  $v \sin i$  values (e.g. HD 65339, HD 176232). In Table 2, we list the derived  $v \sin i$  values along with values found in the literature; the final adopted values correspond to those listed in bold.

It is evident from Table 2 that significant discrepancies exist between  $v \sin i$  values derived in this study and those available in the literature for six mCP stars in the sample

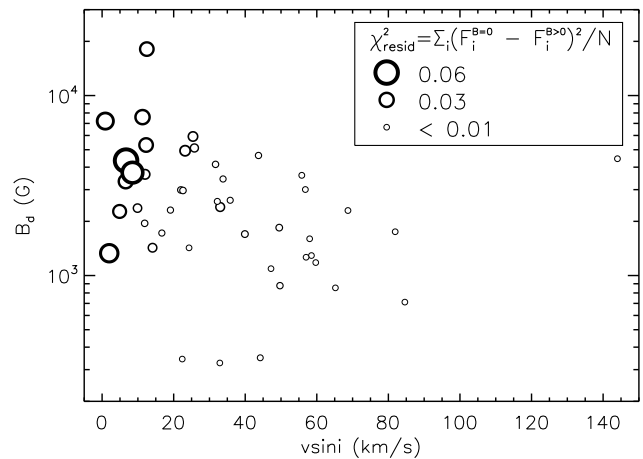


**Figure 7.** Comparisons between spectral models generated with ZEEMAN in which Zeeman broadening is included ( $F^{B>0}$ ) and models in which Zeeman broadening is not included ( $F^{B=0}$ ). We find that, for those fits in which  $\chi^2_{\text{resid}} \lesssim 0.02$ , Zeeman broadening is essentially negligible.

(HD 3980, HD 56022, HD 109026, HD 148898, HD 188041, and HD 223640). In the case of HD 109026, the published  $v \sin i$  value is associated with the primary non-magnetic component, as discussed in Sect. 5.3 and by Alecian et al. (2014). For both HD 3980 and HD 188041, Hubrig, North & Schöller (2007) report lower values of  $v \sin i$  compared to the values derived here. The  $v \sin i$  values derived with and without Zeeman broadening are comparable for these two stars. We note that HD 188041’s radius ( $R = 2.32 \pm 0.19 R_\odot$ ) derived here and its rotational period (223.8 d) and inclination angle ( $70^\circ$ ) reported by Landstreet & Mathys (2000) suggest that  $v \sin i \sim 0.5 \text{ km s}^{-1}$ . The published  $v \sin i$  values of HD 56022, HD 148898, and HD 223640 were obtained by Abt & Morrell (1995a) based on Gaussian fits of the  $\lambda 4476 \text{ Fe I}$  and  $\lambda 4481 \text{ Mg II}$  lines. We computed synthetic models of these lines – both with and without the inclusion of Zeeman broadening – for each of the stars using the published  $v \sin i$  values; comparing the models and the observed spectra used in our study suggest that the published values are incorrect.

The chemical abundance analysis was carried out during both the first and second iterations of our analysis using similar procedures. The effective temperature and surface gravity were fixed at the values derived from the fitting of the photometry (Sect. 5.2.1) and of the Balmer lines (Sect. 5.2.2), respectively, that were performed during the first (current) iteration. The value of  $v \sin i$  was fixed at the value previously derived or adopted. We opted to fix the microturbulence at  $0 \text{ km s}^{-1}$  for two reasons: (1) we found that, for those spectral regions in which certain lines appearing in the observed spectrum but not in the model spectrum,  $v_{\text{mic}}$  would tend to be significantly overestimated ( $\gtrsim 10 \text{ km s}^{-1}$ ) resulting in poor overall fits; and (2)  $v_{\text{mic}}$  is known to be suppressed in mCP stars by the presence of strong surface magnetic fields (e.g. Ryabchikova et al. 1997; Kochukhov et al. 2006). Magnetic fields were included for 14 stars during the second iteration of the chemical abundance analysis; the rationale for this decision to not include magnetic fields for all of the stars is discussed below.

For each spectral region, we selected the elements whose abundances would be fit by referring to the VALD line list and identifying those lines having normalized depths  $> 0.03$ . The abundances of a number of elements selected using this criterion were unable to be fit by the LMA within certain spectral regions, likely as a result of line blending. In these instances, that abundance was fixed at the element's solar value and the LMA was re-run. Typically the abundances of between four and six elements were fit for each spectral region. The final abundances and their uncertainties were derived by taking the median and mean absolute deviation of the values (not including those abundances that were fixed at solar values) derived from each of the 25 to 100 Å width spectral regions; only those chemical abundances which were able to be fit in three or more spectral regions were included in this calculation.

The ZEEMAN LMA requires a prohibitively long time to carry out the polarized radiative transfer calculations for the full sample of mCP stars over spectral windows with widths  $\gtrsim 10$  Å. We attempted to identify those stars that (1) host relatively weak surface magnetic fields and/or (2) exhibit relatively high  $v \sin i$  values such that Zeeman broadening could be neglected without significantly impacting the fitting parameters. This was done by generating models using ZEEMAN with the fitting parameters from the first iteration of the analysis (chemical abundances,  $v \sin i$ , etc.) with the additional inclusion of a dipole magnetic field. The models were generated at the rotational phase corresponding to the maximum width of the lines (the phase at which the impact of Zeeman broadening is greatest). These models were then compared with those generated using the same fitting parameters but without the inclusion of Zeeman broadening. The differences between the synthetic model fluxes in which Zeeman broadening was ( $F^{B>0}$ ) and was not ( $F^{B=0}$ ) included was evaluated by first removing any points corresponding to the continuum ( $F > 0.99$ ) and subsequently calculating the normalized sum of the residuals squared:  $\chi_{\text{resid}}^2 = \sum_i (F_i^{B=0} - F_i^{B>0})^2 / N$  where the sum is carried out over the synthetic flux of each model calculated within a given spectral window and  $N$  corresponds to the number of synthetic flux values within that spectral window.

In Fig. 7, we show  $\chi_{\text{resid}}^2$  as a function of  $v \sin i$  and  $B_d$ . As expected, the models corresponding to the lowest  $v \sin i$  and highest  $B_d$  values exhibit the largest  $\chi_{\text{resid}}^2$  values. In Fig. 8, we show examples of fits obtained with and without the inclusion of magnetic fields. Based on these comparisons, we concluded that Zeeman broadening can be neglected (for the purposes of this investigation) for the 31 stars where  $\chi_{\text{resid}}^2 \lesssim 0.02$ . In Fig. 9, we show examples of fits obtained where Zeeman broadening was found to be non-negligible.

We carried out the spectral modelling of the 5000  $\leq \lambda \leq 5900$  Å regions for the majority of the confirmed mCP stars in the sample. No abundance analysis was carried out for the six stars without available new or archival spectra (HD 12447, HD 49976, HD 54118, HD 64486, HD 103192, and HD 117025 along with the three candidate mCP stars, HD 15717, HD 32576, and HD 217831). No abundance analysis of the SB2 system HD 109026 was carried out due to the significant contamination between the non-magnetic primary and magnetic secondary components in the HARPS spectra. In total, average surface abundances of various elements were derived for 45/52 of the mCP stars. Several

examples of final spectral fits obtained after the first and second iterations are shown in Fig. 8. The four examples span a range of  $v \sin i$  values and approximately represent the range of the quality of the fits obtained during the analysis. The derived chemical abundances are listed in Table 4. We also show four examples of the derived abundance tables in Fig. 10.

### 5.3 HD 109026

HD 109026 is the only double-lined spectroscopic binary system identified amongst the 52 confirmed mCP stars in the sample. The primary component is a slowly pulsating B-type star, which exhibits pulsations with a period of 2.73 d (Waelkens et al. 1998). The cooler secondary component was first discovered by Alecian et al. (2014) based on spectra obtained using HARPSpol. The authors detected variable circularly polarized Zeeman signatures and variable metallic lines, which led them to classify the secondary component as an Ap star. No radial velocity shifts in either the primary or secondary component were reportedly detected over a period of seven nights indicative of an orbital period that is significantly longer than several days.

Various effective temperatures of the system ranging from 15 kK to 17.7 kK have been previously reported based on photometric calibrations (e.g. Molenda-Zakowicz & Polubek 2004; Kochukhov & Bagnulo 2006; Zorec et al. 2009). However, no  $T_{\text{eff}}$  of the cooler magnetic component could be found in the literature. Alecian et al. (2014) attribute their inability to constrain  $T_{\text{eff}}$  to the contamination of the primary component's moderately variable lines with the secondary component's strongly variable lines. We attempted to estimate  $T_{\text{eff}}$  of both components by combining the constraints yielded by (1) SED fitting and (2) spectral Balmer line modelling.

Johnson, Strömberg, Geneva, and 2MASS photometric measurements are available for HD 109026. We attempted to fit the observations using a grid search method in which  $\chi^2$  is calculated for a grid of free parameters allowing the minimal  $\chi^2$  solution to be identified. Unlike the SED fitting method discussed in Sect. 5.2.1, we (1) included contributions from both a primary and secondary component and (2) we did not consider the effects of chemical peculiarities or surface magnetic fields. The metallicity and surface gravity of both components were fixed at  $[M/H] = 0$  and  $\log g = 4.0$  (cgs), respectively. The effective temperatures and radii of both components were free parameters; the primary component's  $T_{\text{eff}}$  and  $R$  were bounded by  $T_{\text{eff,A}}/\text{kK} \in [14, 20]$  and  $R_A/R_\odot \in [3, 5]$  while the secondary component's  $T_{\text{eff}}$  and  $R$  were bounded by  $T_{\text{eff,B}}/\text{kK} \in [8, 15]$  and  $R_B/R_\odot \in [3, 5]$ . Lastly, in order to reduce the number of grid points in the  $\chi^2$  space (and thus, reduce the computation time), we restricted the primary component's luminosity (computed using the Stefan-Boltzmann relation) such that  $L_A/L_B > 1$ . In Fig. 11 we show the two components'  $\chi^2$  distributions in the  $T_{\text{eff}}$  and  $R$  planes associated with the SED modelling. It is apparent that the constraints on the free parameters yielded by the SED modelling alone are poor: similar quality fits are obtained for a wide range of solutions ( $16 \lesssim T_{\text{eff,A}} \lesssim 20$  kK and  $9 \lesssim T_{\text{eff,B}} \lesssim 15$  kK).

The available HARPS Stokes  $I$  spectra of HD 109026 span the H $\gamma$  and H $\beta$  lines. We performed a similar spec-

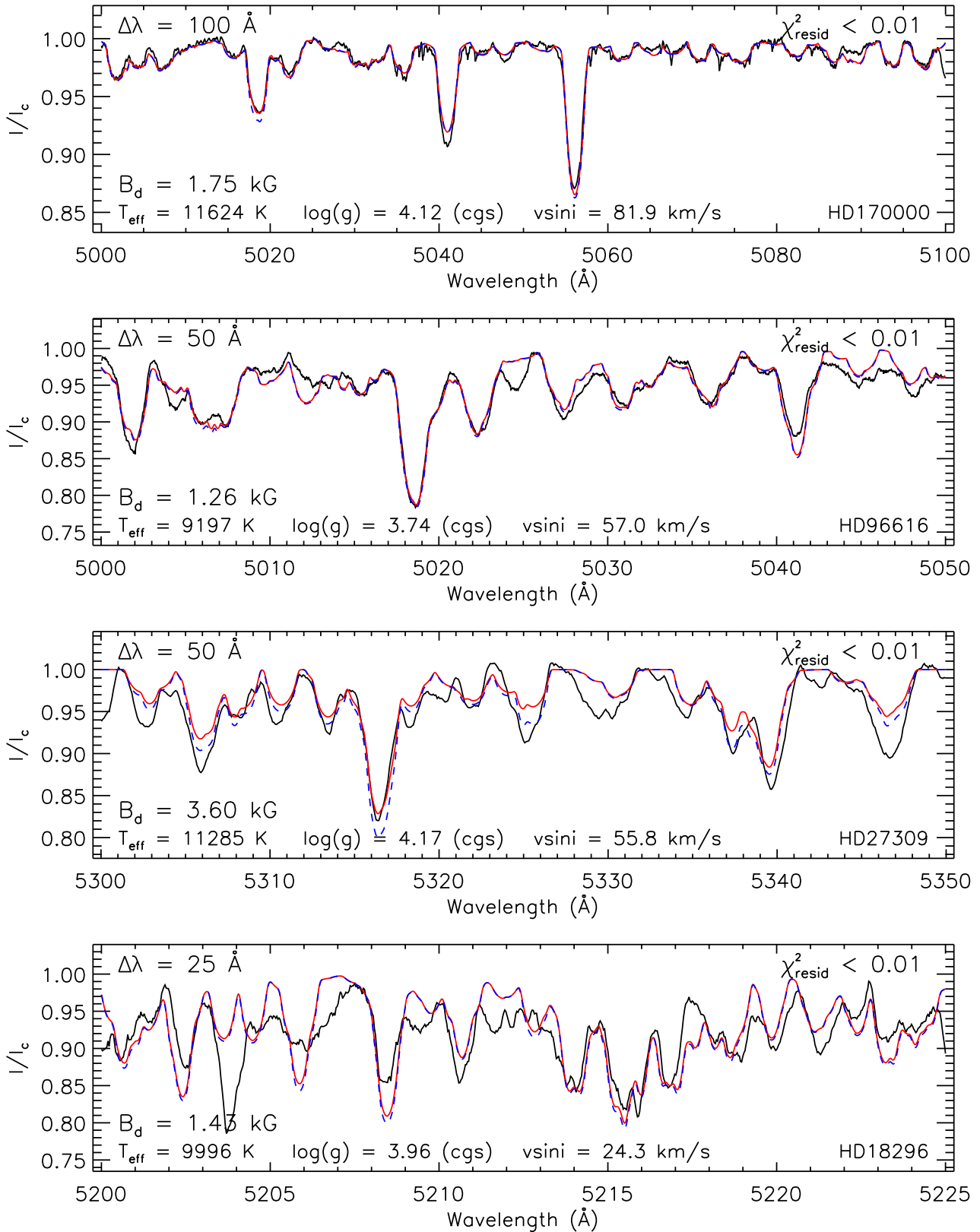


**Figure 8.** Several examples of the fits generated as discussed in Sect. 5.2.3. The black curves correspond to the observed spectra, the red curves correspond to the best-fitting model spectra derived using the ZEEMAN LMA without including Zeeman broadening, and the dashed-blue curves correspond to the spectra generated using ZEEMAN with the same fitting parameters and with Zeeman broadening included. A range of  $v \sin i$  values are represented decreasing from top to bottom. Note that the different widths of the spectral regions shown, which are labeled in the top left of each figure.

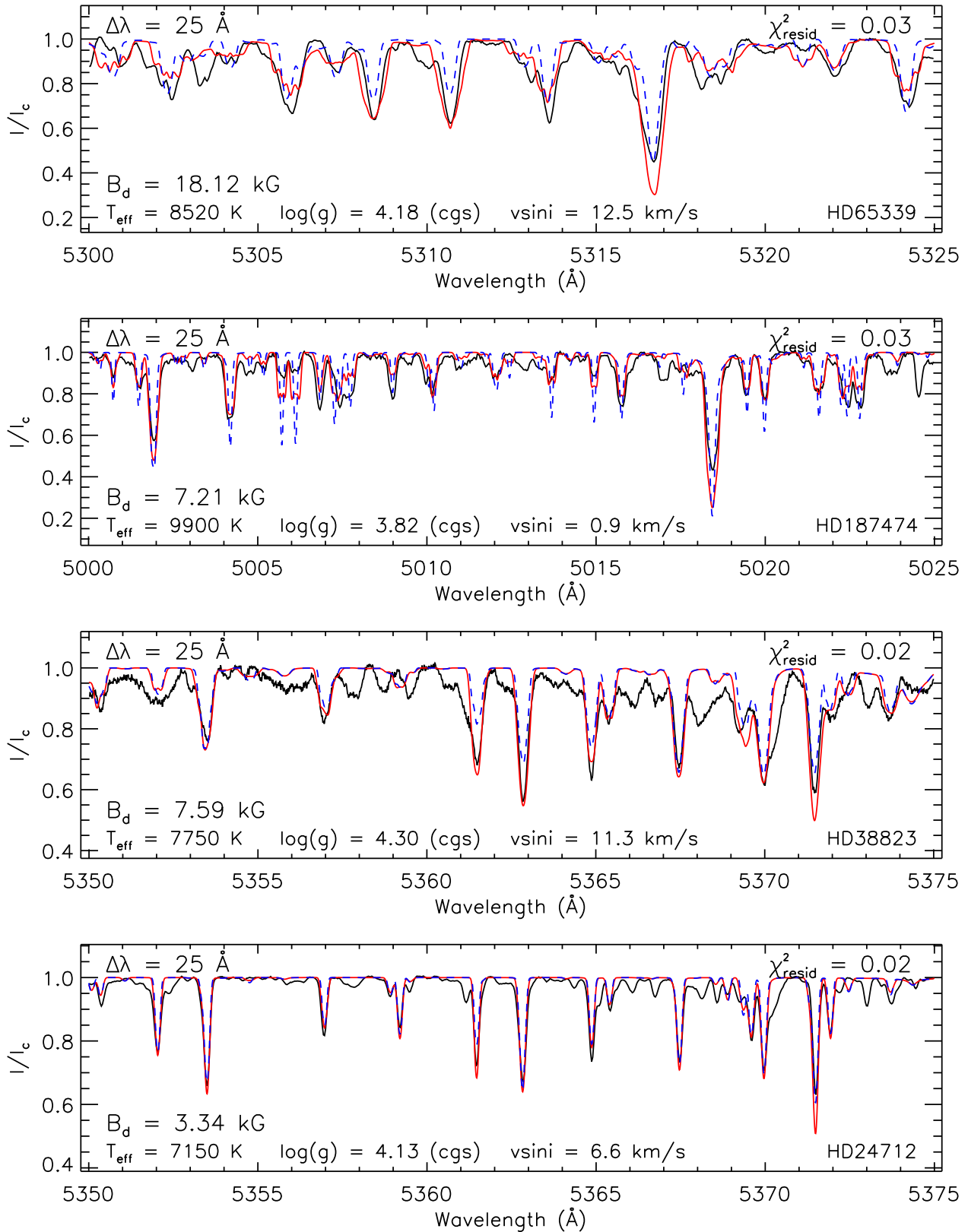


**Figure 9.** Examples of fits generated where a dipole magnetic field was included in the model. The black curves correspond to the observed spectra, the red curves correspond to the best-fitting model spectra derived using the ZEEMAN LMA with Zeeman broadening included, and the dashed-blue curves correspond to the spectra generated using ZEEMAN with the same fitting parameters and no Zeeman broadening included. In each case,  $\chi^2_{\text{resid}} \geq 0.02$  (as shown in Fig. 7) and Zeeman broadening is considered to be non-negligible.

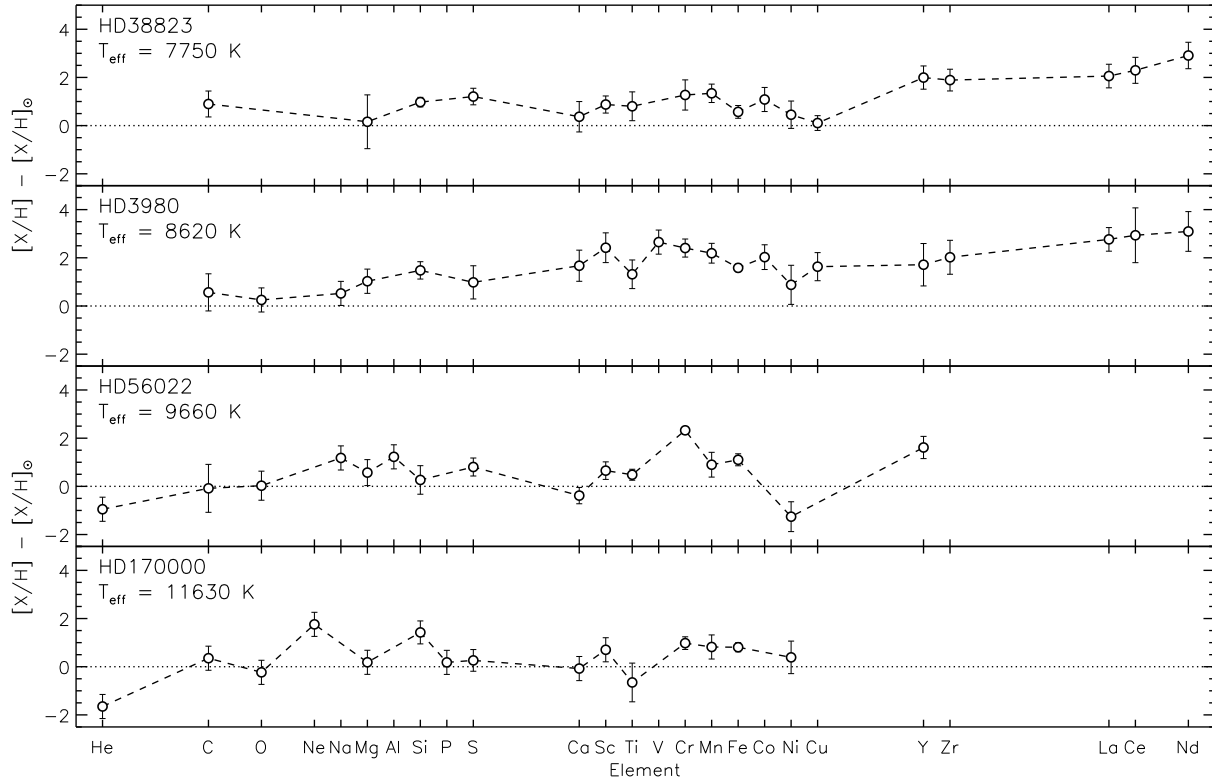


**Figure 10.** Examples of the tables of derived average surface chemical abundances. The examples shown increase in  $T_{\text{eff}}$  from top to bottom.

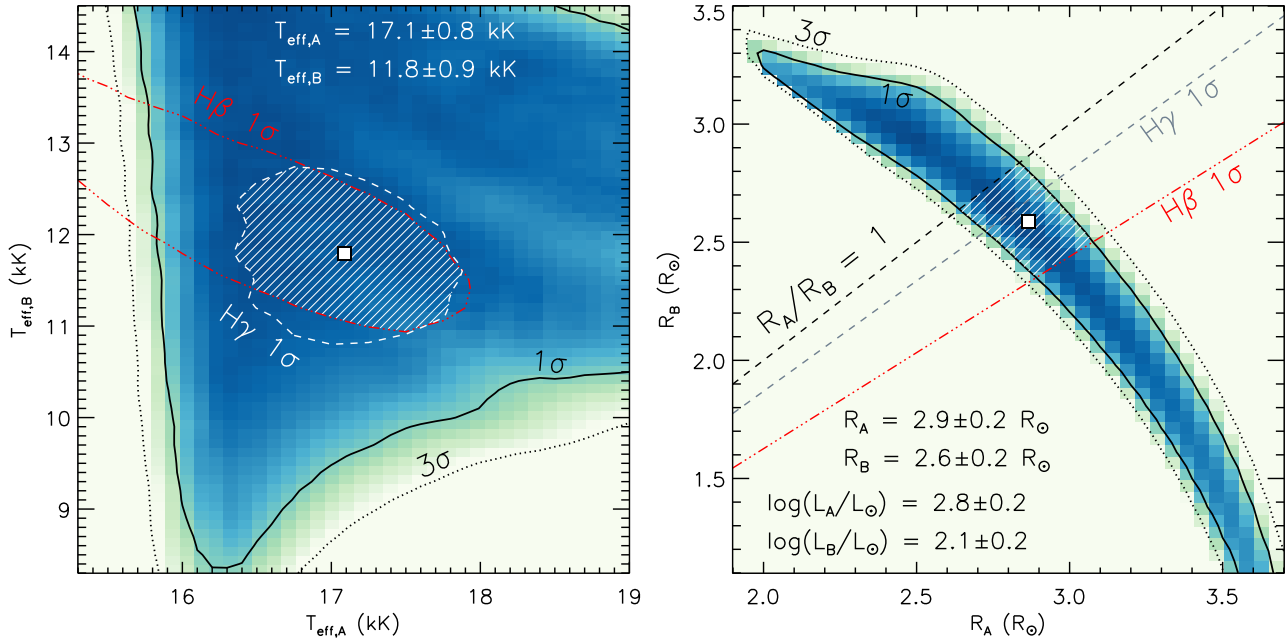


**Figure 11.** The  $\chi^2$  distributions associated with the SED modelling (shown in Fig. 12): the colours correspond to the  $\chi^2$  value increasing from dark to light while the solid and dotted black contours correspond to the  $1\sigma$  and  $3\sigma$  limits, respectively. In both plots, the white hatched regions indicate the regions used to assign final values (marked by white squares) and uncertainties of the plotted parameters. *Left:* Comparisons between the  $T_A - T_B$   $\chi^2$  plane associated with the photometry and the Balmer line modelling. The red dot-dashed and white dashed contours correspond to the  $1\sigma$  limits of the  $H\beta$  and  $H\gamma$  modelling shown in Fig. 13. *Right:* The  $R_A - R_B$   $\chi^2$  plane associated with the photometry. The Balmer line modelling yields constraints on the ratio of the radii ( $R_A/R_B$ ); the  $1\sigma$  upper limits for  $R_A/R_B$  are indicated by the grey dashed and red dot-dashed lines while the dashed black line shows the lower limit of  $R_A/R_B = 1$  enforced during the fitting analysis.

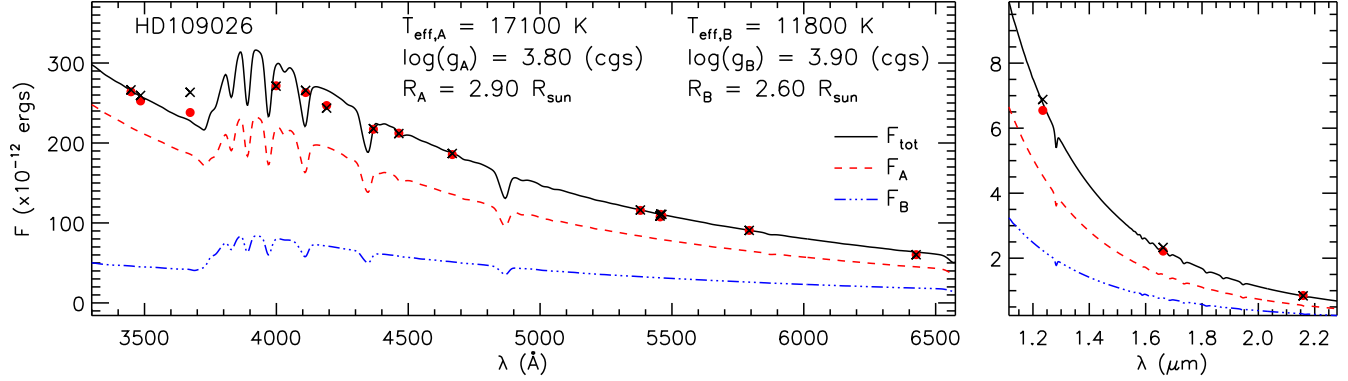


**Figure 12.** The final fit to the observed photometry (filled red circles) of the SB2 system HD 109026. The left panel shows the optical photometry (Johnson, Geneva, and Strömgren) while the right panel shows the 2MASS photometry. The solid black, dashed red, and dot-dashed blue lines correspond to the total, primary component, and secondary (magnetic) component synthetic SEDs. The black ‘X’ symbols correspond to the total synthetic flux of each photometric filter.

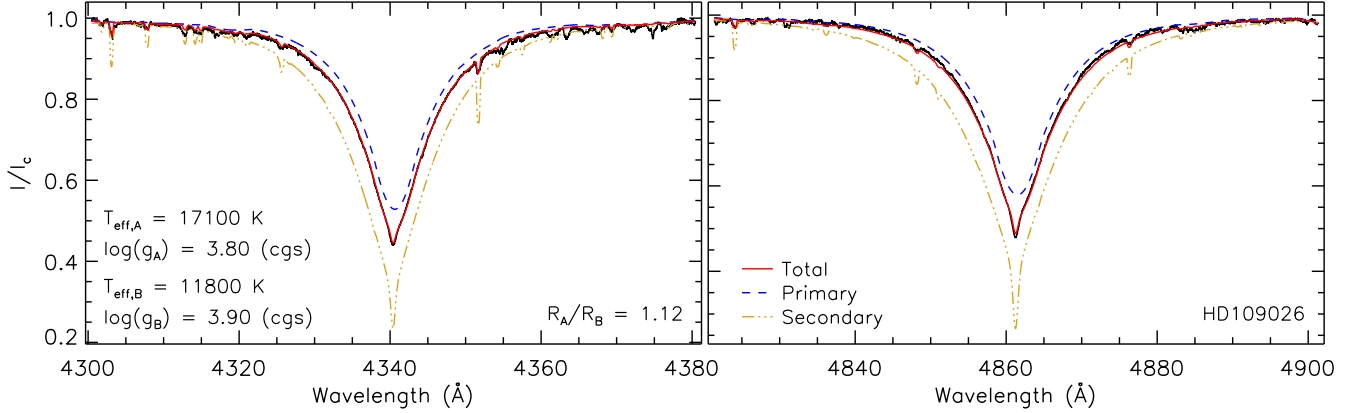


**Figure 13.** The final fits to the observed H $\gamma$  (left) and H $\beta$  (right) profiles (black curves) of the SB2 system HD 109026. The dashed blue, dot-dashed yellow, and solid red curves correspond to the primary, secondary (magnetic), and composite model spectra.

tral line modelling analysis to that presented in Sect. 5.2.2 using the GSSP COMPOSITE module described by Tkachenko (2015). This module functions in the same way as the GSSP SINGLE module used in Sect. 5.2.2 (i.e. by generating a grid of solutions from which the minimal  $\chi^2$  solution can be identified) but allows a spectrum consisting of two components to be fit. We defined a grid of  $T_{\text{eff},A}/\text{kK} \in [14, 19]$ ,  $T_{\text{eff},B}/\text{kK} \in [10, 15]$ ,  $\log g_A \in [3.0, 5.0]$ , and  $\log g_B \in [3.0, 5.0]$  values with increments of  $\Delta T_{\text{eff}} = 100 \text{ K}$  and  $\Delta \log g = 0.1$  (cgs). The  $v \sin i$  values of each component were varied from  $170 - 190 \text{ km s}^{-1}$  in increments of  $1 \text{ km s}^{-1}$  (primary) and  $5 - 25 \text{ km s}^{-1}$  in increments of  $0.5 \text{ km s}^{-1}$  (secondary). We used fixed solar abundancies (i.e. no individual abundancies were varied), and fixed microturbulence values of  $2 \text{ km s}^{-1}$  and  $0 \text{ km s}^{-1}$  for the primary and secondary components, respectively. The contribution of each component to the composite spectrum is primarily determined by the ratio of the luminosities ( $L_A/L_B = [T_A/T_B]^4 [R_A/R_B]^2$ ); we allowed the ratio of the radii,  $R_A/R_B$ , to range from 1 to 3 in increments of 0.05.

The resulting  $\chi^2$  grids associated with the fits to H $\gamma$  and H $\beta$  were then compared with the  $\chi^2$  grids generated during the SED fitting analysis. In Fig. 11 (left), we show the resulting spectral modelling  $1\sigma$  contours associated with

$T_{\text{eff},A}$  and  $T_{\text{eff},B}$  overlaid onto the SED fitting  $T_{\text{eff}}$   $\chi^2$  distribution. In Fig. 11 (right), we show the spectral modelling  $1\sigma$  limits of  $R_A/R_B$  overlaid onto the  $R$  SED fitting  $\chi^2$  distribution. By combining the constraints yielded by both the SED fitting and the Balmer line fitting, we obtain best fitting parameters – corresponding to the centers of the overlapping  $1\sigma$  contours – with large but reasonable  $1\sigma$  errors:  $T_{\text{eff},A} = 17.1 \pm 0.8 \text{ kK}$ ,  $T_{\text{eff},B} = 11.8 \pm 0.9 \text{ kK}$ ,  $R_A = 2.9 \pm 0.2 R_\odot$ , and  $R_B = 2.6 \pm 0.2 R_\odot$ . These values yield luminosities of  $\log L_A/L_\odot = 2.8 \pm 0.2$  and  $\log L_B/L_\odot = 2.1 \pm 0.2$ . In Figures 12 and 13, we show the SED fits and Balmer line fits generated using the derived most probable parameters.

#### 5.4 Hertzsprung-Russell diagram

With the values of  $T_{\text{eff}}$  and  $L$  derived for all of the stars (mCP, candidate mCP, and non-mCP), their masses ( $M$ ) and ages ( $t_{\text{age}}$ ) could be estimated by generating a theoretical Hertzsprung-Russell diagram (HRD) and comparing with evolutionary models. Various theoretical evolutionary tracks spanning a wide range of metallicities and rotation rates are available in the literature (e.g. Schaller et al. 1992; Schaerer et al. 1993; Georgy et al. 2013). Depending on the

**Table 2.** Rotational broadening ( $v \sin i$ ) and surface gravity  $\log g$  derived from spectroscopic measurements. Columns 2, 4, 6, and 8 list the  $v \sin i$  and  $\log g$  values derived in this study; columns 3 and 7 list  $v \sin i$  values obtained from the literature. The bold  $v \sin i$  values correspond to the final adopted values used in the final spectral models and in the calculation of the magnetic parameters in Paper II. References for the published  $v \sin i$  values are listed in the table's footer.

HD	$(v \sin i)_{\text{obs}}$ (km s <sup>-1</sup> )	$(v \sin i)_{\text{pub}}$ (km s <sup>-1</sup> )	$\log(g)_{\text{obs}}$ (cgs)	HD	$(v \sin i)_{\text{obs}}$ (km s <sup>-1</sup> )	$(v \sin i)_{\text{pub}}$ (km s <sup>-1</sup> )	$\log(g)_{\text{obs}}$ (cgs)
(1)	(2)	(3)	(4)	(5)	(6)	(7)	(8)
3980	<b>25.4 ± 1.7</b>	15.0 ± 3.0 <sup>a</sup>	4.04 <sup>+0.78</sup> <sub>-0.42</sub>	112413	<b>17.3 ± 2.2</b>	-	3.89 <sup>+0.77</sup> <sub>-0.37</sub>
11502	<b>56.8 ± 1.7</b>	-	4.04 <sup>+0.96</sup> <sub>-0.50</sub>	117025	-	-	-
12446	-	<b>56.0 ± 3.0</b> <sup>b</sup>	-	118022	<b>12.0 ± 0.7</b>	12.0 ± 1.0 <sup>k</sup>	4.11 <sup>+0.89</sup> <sub>-0.42</sub>
15089	<b>49.5 ± 2.8</b>	-	-	119213	<b>35.8 ± 3.8</b>	-	4.17 <sup>+0.83</sup> <sub>-0.46</sub>
15144	<b>12.0 ± 0.9</b>	13.0 ± 1.0 <sup>c</sup>	-	120198	<b>58.0 ± 1.5</b>	-	3.83 <sup>+0.71</sup> <sub>-0.17</sub>
18296	<b>24.3 ± 2.4</b>	-	3.33 <sup>+0.97</sup> <sub>-0.33</sub>	124224	<b>144 ± 5</b>	-	4.06 <sup>+0.36</sup> <sub>-0.12</sub>
24712	<b>6.6 ± 0.6</b>	-	3.80 <sup>+1.20</sup> <sub>-0.80</sub>	128898	<b>14.1 ± 0.5</b>	14.0 ± 1.0 <sup>l</sup>	> 4.22
27309	<b>55.8 ± 2.4</b>	-	-	130559	<b>18.6 ± 1.6</b>	-	3.84 <sup>+1.09</sup> <sub>-0.49</sub>
29305	<b>44.2 ± 1.9</b>	-	3.97 <sup>+0.47</sup> <sub>-0.31</sub>	137909	<b>9.5 ± 0.4</b>	-	3.25 <sup>+1.33</sup> <sub>-0.25</sub>
38823	<b>11.3 ± 1.9</b>	-	4.30 <sup>+0.51</sup> <sub>-1.29</sub>	137949	<b>9.7 ± 0.5</b>	-	3.30 <sup>+1.38</sup> <sub>-0.30</sub>
40312	<b>58.5 ± 2.5</b>	57.0 ± 10.0 <sup>d</sup>	3.41 <sup>+0.49</sup> <sub>-0.21</sub>	140160	<b>59.7 ± 2.1</b>	-	4.00 <sup>+0.24</sup> <sub>-0.16</sub>
49976	-	<b>31.0 ± 3.0</b> <sup>e</sup>	-	140728	<b>68.7 ± 3.2</b>	65.0 <sup>m</sup>	3.69 <sup>+0.53</sup> <sub>-0.21</sub>
54118	-	<b>34.0 ± 2.0</b> <sup>f</sup>	-	148112	<b>47.2 ± 3.0</b>	-	3.45 <sup>+0.67</sup> <sub>-0.25</sub>
56022	<b>84.6 ± 7.4</b>	28.0 ± 8.0 <sup>b</sup>	3.93 <sup>+0.64</sup> <sub>-0.16</sub>	148898	<b>32.2 ± 1.4</b>	51.0 ± 8.0 <sup>m</sup>	3.85 <sup>+0.65</sup> <sub>-0.69</sub>
62140	<b>25.8 ± 1.0</b>	-	3.70 <sup>+1.30</sup> <sub>-0.70</sub>	151199	<b>49.7 ± 1.9</b>	-	4.02 <sup>+0.22</sup> <sub>-0.12</sub>
64486	-	-	-	152107	<b>23.2 ± 1.4</b>	-	4.10 <sup>+0.61</sup> <sub>-0.19</sub>
65339	13.3 ± 2.7	<b>12.5 ± 0.5</b> <sup>g</sup>	4.18 <sup>+0.67</sup> <sub>-0.25</sub>	170000	<b>81.9 ± 1.6</b>	-	4.11 <sup>+0.27</sup> <sub>-0.13</sub>
72968	<b>16.1 ± 0.8</b>	-	3.83 <sup>+0.97</sup> <sub>-0.33</sub>	176232	2.1 ± 0.7	<b>2.0 ± 0.5</b> <sup>n</sup>	4.00 ± 1.00
74067	<b>33.8 ± 2.8</b>	33.0 ± 1.0 <sup>h</sup>	4.13 <sup>+0.69</sup> <sub>-0.31</sub>	187474	<b>0.9 ± 0.6</b>	-	3.82 <sup>+1.18</sup> <sub>-0.58</sub>
83368	33.8 ± 1.0	<b>33.0 ± 0.5</b> <sup>g</sup>	3.56 <sup>+0.24</sup> <sub>-0.56</sub>	188041	<b>6.7 ± 0.5</b>	4.0 <sup>a</sup>	4.36 <sup>+0.64</sup> <sub>-0.76</sub>
96616	<b>57.0 ± 2.5</b>	56.0 ± 2.5 <sup>i</sup>	3.72 <sup>+0.44</sup> <sub>-0.16</sub>	201601	<b>7.0 ± 0.5</b>	-	3.85 <sup>+0.51</sup> <sub>-0.85</sub>
103192	-	<b>72.0</b> <sup>b</sup>	-	203006	<b>43.7 ± 1.7</b>	-	3.73 <sup>+0.29</sup> <sub>-0.23</sub>
108662	<b>22.0 ± 1.7</b>	-	3.72 <sup>+0.26</sup> <sub>-0.16</sub>	217522	<b>4.9 ± 0.6</b>	-	< 4.20
108945	<b>65.2 ± 3.8</b>	-	3.85 <sup>+0.11</sup> <sub>-0.15</sub>	220825	<b>39.9 ± 2.2</b>	-	3.94 <sup>+0.12</sup> <sub>-0.18</sub>
109026	<b>12.0 ± 1.5</b>	188 ± 10 <sup>j</sup>	3.90 ± 0.30	221760	<b>22.4 ± 0.7</b>	-	3.65 <sup>+0.41</sup> <sub>-0.09</sub>
112185	<b>32.9 ± 1.4</b>	-	3.66 <sup>+0.96</sup> <sub>-0.14</sub>	223640	<b>31.7 ± 1.4</b>	20.0 ± 5.0 <sup>m</sup>	3.92 <sup>+0.42</sup> <sub>-0.22</sub>

<sup>a</sup> Hubrig, North & Schöller (2007), <sup>b</sup> Abt (2001), <sup>c</sup> Aurière et al. (2007), <sup>d</sup> Rice & Wehlau (1990)

<sup>e</sup> Pilachowski, Bonsack & Wolff (1974), <sup>f</sup> Donati et al. (1997), <sup>g</sup> Kochukhov et al. (2004), <sup>h</sup> Royer, Grenier & Zorec (2002)

<sup>i</sup> Hoffleit & Warren (1995), <sup>j</sup> Brown & Verschueren (1997), <sup>k</sup> Khalack & Wade (2006), <sup>l</sup> Reiners & Schmitt (2003)

<sup>m</sup> Abt & Morrell (1995a), <sup>n</sup> Kochukhov et al. (2002)

choice of models, the derived masses and, in particular, the derived ages of the stars can vary substantially.

Although our analysis includes a derivation of most of the mCP stars' surface chemical compositions, it is understood that these values are not representative of their bulk metallicities (e.g. Michaud 1970, 1980). Studies of the Sun's metallicity as well as that of nearby B-type stars (Przybilla, Nieva & Butler 2008) and star-forming H II regions (e.g. Esteban et al. 2004) suggest that  $Z \approx 0.014$  within the solar neighbourhood (Asplund et al. 2009). The Geneva-Copenhagen survey (Nordström et al. 2004; Casagrande et al. 2011), which derived the metallicities of more than 16 000 F-, G-, and K-type stars in the Hipparcos Catalogue, report a similar value within the solar neighbourhood: the 9 605 stars within 100 pc with derived  $[M/H]$  values exhibit an approximately Gaussian distribution with mean and sigma values of  $-0.04$  and  $0.15$ , respectively. No significant change in  $[M/H]$  is found as a function of distance within

100 pc. Based on these results, we adopted metallicities of  $[M/H] = 0.0$  with a  $2 \sigma$  uncertainty of  $0.3$  ( $Z = 0.014 \pm 0.009$ ) for all of the stars (both mCP and non-mCP) in the sample.

Magnetic F-, A-, and B-type MS stars are typically known to have relatively low equatorial rotational velocities ( $v_{\text{eq}}$ ) (e.g. Abt & Morrell 1995b; Netopil et al. 2017), however, the  $v_{\text{eq}}$  values exhibited by their non-mCP counterparts vary widely. We estimated the non-mCP sub-sample's typical ratio of  $v_{\text{eq}}$  to the critical rotational velocity (i.e. the break-up rotational velocity,  $v_{\text{crit}}$ ) by first compiling the  $v \sin i$  and  $T_{\text{eff}}$  values of MS A-type stars reported by Ammler-von Eiff & Reiners (2012) and Zorec & Royer (2012). We then estimated  $v_{\text{crit}}$  for each of the 2 835 catalogue entries using the non-rotating, solar metallicity evolutionary tracks computed by Ekström et al. (2012). A Monte Carlo (MC) simulation was then performed in which, for each of the 1 000 steps that were carried out, inclination angles were randomly assigned for each star under the assump-

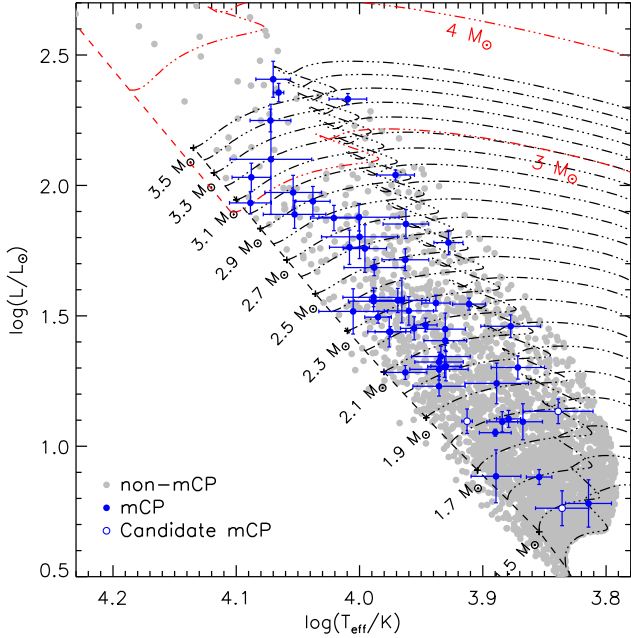


**Figure 14.** Theoretical HRD of the sample of non-mCP stars (grey points), the confirmed mCP stars (blue filled circles), and the candidate mCP stars (blue open circles). The black and red dash-dotted curves correspond to the solar metallicity low- and high-mass evolutionary tracks computed by Mowlavi et al. (2012) and Ekström et al. (2012), respectively.

tion that the rotational axes are randomly oriented in space. Our results suggest that we can expect the subsample of non-mCP stars to have a median  $v_{\text{eq}}/v_{\text{crit}}$  of approximately 0.3 and for 68 per cent of the sample to have  $v_{\text{eq}}/v_{\text{crit}} \lesssim 0.4$ .

We used several grids of evolutionary models computed with a range of metallicities to derive the stellar masses and ages along with their uncertainties. Mowlavi et al. (2012) computed 6 dense grids of evolutionary tracks corresponding to metallicities of 0.006, 0.01, 0.014, 0.02, 0.03, and 0.04; each grid contains 39 tracks with  $0.5 \leq M/M_{\odot} \leq 3.5$ . Ekström et al. (2012) computed four larger, lower density grids having metallicities of 0.002 and 0.014, both with rotation ( $v_{\text{eq}}/v_{\text{crit}} = 0.4$ ) and without rotation; each grid contains 24 tracks corresponding to a wide range of masses ( $0.8 \leq M/M_{\odot} \leq 120$ ). Comparing these grids, it is evident that  $T_{\text{eff}}$  of the terminal-age MS (TAMS) decreases significantly for those tracks associated with a high metallicity ( $Z = 0.03$ ) and/or fast rotation rate ( $v_{\text{eq}}/v_{\text{crit}} = 0.4$ ) relative to the non-rotating solar metallicity models. We linearly interpolated the grids computed by Mowlavi et al. (2012) in order to generate a  $Z = 0.023$  grid (corresponding to the adopted high metallicity limit inferred from the Geneva-Copenhagen survey) and similarly interpolated the grids computed by Ekström et al. (2012) in order to generate a solar metallicity,  $v_{\text{eq}}/v_{\text{crit}} = 0.3$  grid (corresponding to the estimated typical rotational velocity of the non-mCP stars). We found that the  $Z = 0.023$  models yielded a moderately cooler TAMS compared to the rotating models; therefore, since the width of the MS is more strongly affected by an increase in  $Z$  compared to an increase in  $v_{\text{eq}}/v_{\text{crit}}$ , we opted to use only the available non-rotating models. We used the grids computed by Mowlavi et al. (2012) for

the stars with  $M < 3.5 M_{\odot}$  along with the non-rotating grids computed by Ekström et al. (2012) for the stars with  $M \geq 3.5 M_{\odot}$ . As a consequence, the derived uncertainties in  $M$  and  $t_{\text{age}}$  associated with the lower-mass stars incorporate both low and high metallicities ( $0.006 \leq Z \leq 0.023$ ) while those of the high-mass stars only incorporate low metallicities ( $0.005 \leq Z \leq 0.014$ ).

At this point in the analysis, we applied three cuts to the sample of non-mCP stars. All non-mCP stars with derived masses  $< 1.4 M_{\odot}$  were removed since this approximately corresponds to the least massive mCP star in the sample (HD 217522, which has a mass of  $1.48 M_{\odot}$ ). This cut was applied using the  $Z = 0.014$  grid of evolutionary tracks (Ekström et al. 2012). The next two cuts removed all stars positioned (1) below the zero-age MS (ZAMS, identified using the  $Z = 0.023$  evolutionary models computed by Mowlavi et al. 2012) – these stars are discussed below – and (2) above the coolest point along the MS (identified using the  $Z = 0.014$  models computed by Ekström et al. 2012). These stars have evolved off of the MS and are associated with various phenomena (e.g. rapid structural changes) that are outside the scope of this study. The three cuts reduced the total number of non-mCP stars in the sample from 21 665 to 3 141. The HRD containing the confirmed mCP, candidate mCP, and non-mCP stars composing the sample is shown in Fig. 14 along with the adopted solar metallicity evolutionary tracks.

We note that 150 non-mCP stars – along with three candidate mCP stars (HD 107452, HD 122811, and HD 177880B) – exhibit  $\log T_{\text{eff}}/K \gtrsim 3.9$  and  $\log L/L_{\odot} \lesssim 0.3$  and are therefore positioned well below the ZAMS associated with the  $Z = 0.006$  grid of evolutionary tracks. It is unlikely that errors in the derived  $T_{\text{eff}}$  and/or  $\log L$  alone could reposition these stars below the MS this significantly. Wraight et al. (2012) note that HD 107452 is a binary system and suggest that the parallax reported within the Hipparcos Catalogue may have been affected by this. Based on the derived effective temperatures of these three candidate mCP stars, we find that the distances would need to be increased by factors of approximately 2.5 to 4.5 in order for them to be positioned near the ZAMS (this estimate does not consider the flux contributed from the binary companion, which would reduce the factor). An analysis of specific binary systems presented by Pourbaix & Jorissen (2000) demonstrates that the parallax angles measured using Hipparcos can be overestimated by a factor  $\lesssim 3$  if the orbital motion of a star within the system is not accounted for, which suggests that the aforementioned stars in this sample may be similarly affected.

Each sample star’s most probable  $M$  and  $t_{\text{age}}$  were derived by linearly interpolating the adopted solar metallicity evolutionary tracks. Their associated uncertainties were estimated by carrying out the following MC analysis. A large number ( $\gtrsim 1000$ ) data points consisting of  $T_{\text{eff}}$ ,  $L$ , and  $Z$  values were generated by randomly sampling from Gaussian distributions defined by each parameter’s most probable values and uncertainties:  $T_{\text{eff}}$ ,  $\sigma_{T_{\text{eff}}}$ ,  $L$ , and  $\sigma_L$  were derived in Section 5.2.1 while  $Z$  and  $\sigma_Z$  were inferred from the Geneva-Copenhagen survey (this MC HRD method corresponds to a simplified version of that carried out by Shultz et al., in prep). We then derived the corresponding masses and ages for each of those data points found to overlap with

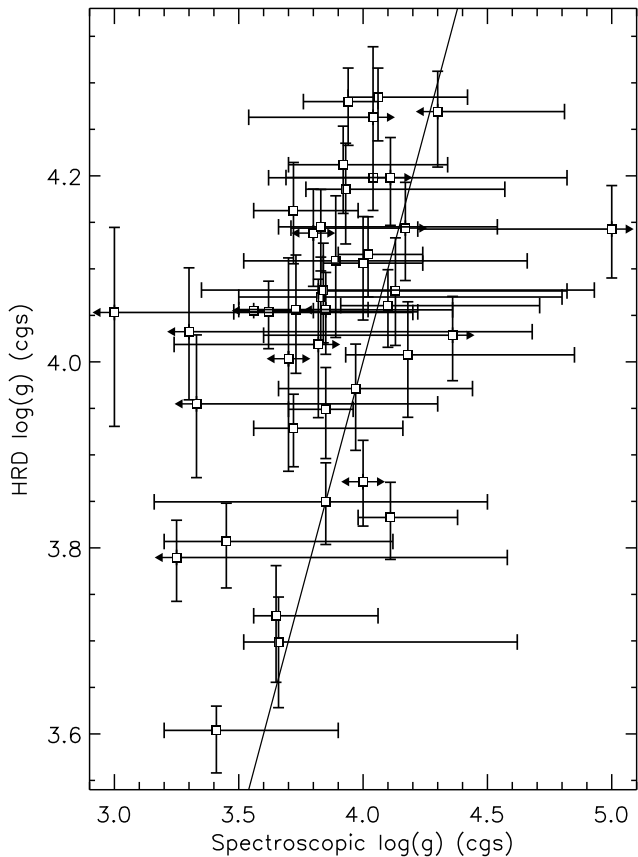


**Figure 15.** Surface gravity derived from H $\beta$  and H $\gamma$  (spectroscopic  $\log g$ ) compared with the values derived from each star’s position on the theoretical HRD (HRD  $\log g$ ). Each square symbol corresponds to the best-fitting/most probable  $\log g$  while the arrows indicate uncertainties that extend beyond the  $3.0 \leq \log g \leq 5.0$  (cgs) range permitted during the fitting analysis. The black line corresponds to where the spectroscopic  $\log g$  equals the HRD  $\log g$ .

the evolutionary model grids. The uncertainties in  $M$  and  $t_{\text{age}}$  were determined from the widths of the resulting distributions. No masses and ages could be derived for those non-mCP stars positioned below the solar metallicity evolutionary grid’s MS using their most probable  $T_{\text{eff}}$  and  $L$  values derived in Section 5.1. In these cases,  $M$  and  $t_{\text{age}}$  were assigned the values associated with the nearest valid  $T_{\text{eff}}$ ,  $L$ , and  $Z$  obtained during the MC error analysis.

In Table 3, we list (1) the  $T_{\text{eff}}$ ,  $R$ , and  $\log L$  values derived from the spectroscopic and photometric observations, and (2) the  $M$ ,  $\log g$ ,  $\log t_{\text{age}}$ , and  $\tau$  values derived using the evolutionary models; the 52 confirmed mCP stars and the 3 candidate mCP stars are included in this table.

## 6 RESULTS

### 6.1 Confirmation of $T_{\text{eff}}$

The modelling of H $\gamma$  and H $\beta$  carried out in Sect. 5.2.2 is, to some extent, degenerate in  $\log g$  and  $T_{\text{eff}}$ : if the value of  $\log g$  derived by fitting the Balmer lines is found to be inaccurate,  $T_{\text{eff}}$  may also be inaccurate despite having obtained a high-quality fit. In order to assess the accuracy of

**Table 3.** Derived fundamental parameters for the 52 confirmed mCP stars and 3 candidate mCP stars (HD 15717, HD 32576, and HD 217831) in the sample. Columns (1) through (4) list parameters derived from the spectroscopic and photometric observations. Columns (5) through (8) list parameters derived using the evolutionary models generated by Mowlavi et al. (2012) and Ekström et al. (2012).

HD (1)	$T_{\text{eff}}$ (K) (2)	$R$ ( $R_{\odot}$ ) (3)	$\log L/L_{\odot}$ (4)	$M$ ( $M_{\odot}$ ) (5)	$\log(g)_{\text{HRD}}$ (6)	$\log t/\text{Gyrs}$ (7)	$\tau$ (8)
3980	8620 ± 420	1.85 ± 0.19	1.23 ± 0.04	1.96 <sup>+0.13</sup> <sub>-0.21</sub>	4.20 ± 0.10	8.67 <sup>+0.30</sup> <sub>-0.70</sub>	0.41 <sup>+0.35</sup> <sub>-0.33</sub>
11502	10120 ± 650	1.86 ± 0.31	1.52 ± 0.09	2.36 <sup>+0.17</sup> <sub>-0.29</sub>	4.27 <sup>+0.10</sup> <sub>-0.15</sub>	8.18 <sup>+0.52</sup> <sub>-0.76</sub>	0.23 <sup>+0.45</sup> <sub>-0.19</sub>
12446	10000 ± 710	2.66 ± 0.45	1.80 ± 0.08	2.64 <sup>+0.21</sup> <sub>-0.28</sub>	4.01 ± 0.14	8.52 <sup>+0.16</sup> <sub>-0.27</sub>	0.68 <sup>+0.22</sup> <sub>-0.29</sub>
15089	8530 ± 270	2.06 ± 0.16	1.30 ± 0.04	2.02 <sup>+0.14</sup> <sub>-0.22</sub>	4.12 <sup>+0.07</sup> <sub>-0.08</sub>	8.76 <sup>+0.20</sup> <sub>-0.27</sub>	0.56 <sup>+0.27</sup> <sub>-0.24</sub>
15144	8510 ± 240	2.07 ± 0.17	1.31 ± 0.06	2.02 <sup>+0.15</sup> <sub>-0.22</sub>	4.11 <sup>+0.07</sup> <sub>-0.08</sub>	8.77 <sup>+0.19</sup> <sub>-0.24</sub>	0.57 <sup>+0.26</sup> <sub>-0.23</sub>
15717	6850 ± 1020	1.70 ± 0.22	0.76 ± 0.20	1.49 <sup>+0.12</sup> <sub>-0.24</sub>	4.15 <sup>+0.11</sup> <sub>-0.13</sub>	9.17 <sup>+0.35</sup> <sub>-0.50</sub>	0.63 <sup>+0.49</sup> <sub>-0.42</sub>
18296	10010 ± 750	2.89 ± 0.46	1.88 ± 0.05	2.74 <sup>+0.19</sup> <sub>-0.27</sub>	3.95 ± 0.14	8.52 <sup>+0.13</sup> <sub>-0.21</sub>	0.74 <sup>+0.20</sup> <sub>-0.24</sub>
24712	7150 ± 170	1.80 ± 0.11	0.88 ± 0.03	1.60 <sup>+0.10</sup> <sub>-0.16</sub>	4.13 <sup>+0.06</sup> <sub>-0.07</sub>	9.06 <sup>+0.20</sup> <sub>-0.22</sub>	0.60 <sup>+0.30</sup> <sub>-0.25</sub>
27309	11290 ± 660	2.30 ± 0.31	1.89 ± 0.05	2.87 <sup>+0.20</sup> <sub>-0.31</sub>	4.17 <sup>+0.11</sup> <sub>-0.13</sub>	8.21 <sup>+0.30</sup> <sub>-0.73</sub>	0.41 ± 0.33
29305	11810 ± 450	3.19 ± 0.28	2.25 ± 0.04	3.41 <sup>+0.09</sup> <sub>-0.32</sub>	3.96 <sup>+0.07</sup> <sub>-0.08</sub>	8.26 <sup>+0.13</sup> <sub>-0.08</sub>	0.72 <sup>+0.18</sup> <sub>-0.12</sub>
32576	8180 ± 240	1.76 ± 0.10	1.10 ± 0.14	1.83 <sup>+0.13</sup> <sub>-0.20</sub>	4.21 <sup>+0.05</sup> <sub>-0.07</sub>	8.74 <sup>+0.28</sup> <sub>-0.39</sub>	0.40 <sup>+0.34</sup> <sub>-0.24</sub>
38823	7750 ± 360	1.54 ± 0.23	0.88 ± 0.10	1.65 <sup>+0.12</sup> <sub>-0.20</sub>	4.28 <sup>+0.07</sup> <sub>-0.13</sub>	8.58 <sup>+0.56</sup> <sub>-0.76</sub>	0.21 <sup>+0.52</sup> <sub>-0.17</sub>
40312	10220 ± 360	4.68 ± 0.34	2.33 ± 0.02	3.24 <sup>+0.23</sup> <sub>-0.25</sub>	3.61 <sup>+0.08</sup> <sub>-0.07</sub>	8.46 <sup>+0.02</sup> <sub>-0.10</sub>	1.00 <sup>+0.01</sup> <sub>-0.06</sub>
49976	9460 ± 380	1.95 ± 0.20	1.44 ± 0.06	2.22 <sup>+0.15</sup> <sub>-0.25</sub>	4.20 <sup>+0.08</sup> <sub>-0.10</sub>	8.48 <sup>+0.32</sup> <sub>-0.62</sub>	0.38 <sup>+0.35</sup> <sub>-0.29</sub>
54118	10910 ± 350	2.61 ± 0.24	1.94 ± 0.06	2.89 <sup>+0.20</sup> <sub>-0.29</sub>	4.07 ± 0.09	8.36 <sup>+0.17</sup> <sub>-0.22</sub>	0.60 <sup>+0.23</sup> <sub>-0.22</sub>
56022	9660 ± 240	2.00 ± 0.10	1.50 ± 0.02	2.29 <sup>+0.15</sup> <sub>-0.24</sub>	4.20 <sup>+0.06</sup> <sub>-0.07</sub>	8.45 <sup>+0.29</sup> <sub>-0.43</sub>	0.39 <sup>+0.32</sup> <sub>-0.24</sub>
62140	7740 ± 460	2.32 ± 0.33	1.24 ± 0.08	1.92 <sup>+0.14</sup> <sub>-0.25</sub>	3.99 ± 0.13	8.95 ± 0.19	0.74 ± 0.24
64486	10490 ± 460	2.61 ± 0.28	1.88 ± 0.05	2.77 <sup>+0.19</sup> <sub>-0.28</sub>	4.05 <sup>+0.09</sup> <sub>-0.10</sub>	8.43 <sup>+0.16</sup> <sub>-0.23</sub>	0.63 <sup>+0.22</sup> <sub>-0.24</sub>
65339	8520 ± 320	2.43 ± 0.23	1.45 ± 0.06	2.16 <sup>+0.15</sup> <sub>-0.22</sub>	4.00 ± 0.09	8.79 <sup>+0.13</sup> <sub>-0.15</sub>	0.71 ± 0.19
72968	9310 ± 490	2.32 ± 0.26	1.56 ± 0.05	2.32 <sup>+0.16</sup> <sub>-0.25</sub>	4.07 ± 0.11	8.63 <sup>+0.18</sup> <sub>-0.28</sub>	0.60 <sup>+0.25</sup> <sub>-0.27</sub>
74067	10190 ± 380	2.44 ± 0.25	1.76 ± 0.07	2.62 <sup>+0.18</sup> <sub>-0.28</sub>	4.08 ± 0.09	8.47 <sup>+0.18</sup> <sub>-0.26</sub>	0.58 ± 0.25
83368	7660 ± 220	2.00 ± 0.15	1.09 ± 0.04	1.78 <sup>+0.12</sup> <sub>-0.17</sub>	4.09 <sup>+0.07</sup> <sub>-0.08</sub>	8.97 <sup>+0.15</sup> <sub>-0.20</sub>	0.62 <sup>+0.28</sup> <sub>-0.21</sub>
96616	9180 ± 400	2.85 ± 0.28	1.72 ± 0.04	2.48 <sup>+0.16</sup> <sub>-0.24</sub>	3.93 <sup>+0.09</sup> <sub>-0.10</sub>	8.66 ± 0.12	0.78 ± 0.17
103192	11750 ± 380	3.86 ± 0.38	2.41 ± 0.07	3.65 <sup>+0.08</sup> <sub>-0.53</sub>	3.83 <sup>+0.06</sup> <sub>-0.11</sub>	8.25 <sup>+0.13</sup> <sub>-0.03</sub>	0.89 <sup>+0.09</sup> <sub>-0.05</sub>
108662	9740 ± 460	2.11 ± 0.21	1.56 ± 0.04	2.36 <sup>+0.16</sup> <sub>-0.25</sub>	4.16 ± 0.10	8.49 <sup>+0.27</sup> <sub>-0.48</sub>	0.46 <sup>+0.32</sup> <sub>-0.29</sub>
108945	8670 ± 230	2.64 ± 0.16	1.55 ± 0.03	2.27 <sup>+0.14</sup> <sub>-0.22</sub>	3.95 <sup>+0.06</sup> <sub>-0.07</sub>	8.76 ± 0.10	0.76 <sup>+0.17</sup> <sub>-0.14</sub>
109026	11800 ± 900	2.68 ± 0.82	2.10 ± 0.21	3.19 <sup>+0.29</sup> <sub>-0.40</sub>	4.08 <sup>+0.20</sup> <sub>-0.22</sub>	8.22 <sup>+0.21</sup> <sub>-0.72</sub>	0.56 <sup>+0.31</sup> <sub>-0.46</sub>
112185	9350 ± 330	3.99 ± 0.28	2.04 ± 0.02	2.94 <sup>+0.15</sup> <sub>-0.41</sub>	3.70 <sup>+0.07</sup> <sub>-0.10</sub>	8.54 <sup>+0.12</sup> <sub>-0.05</sub>	0.94 <sup>+0.07</sup> <sub>-0.08</sub>
112413	11320 ± 600	2.52 ± 0.31	1.97 ± 0.07	2.97 <sup>+0.22</sup> <sub>-0.32</sub>	4.11 ± 0.11	8.28 <sup>+0.22</sup> <sub>-0.43</sub>	0.53 <sup>+0.28</sup> <sub>-0.31</sub>
117025	8590 ± 470	2.12 ± 0.25	1.34 ± 0.04	2.06 <sup>+0.14</sup> <sub>-0.21</sub>	4.10 ± 0.11	8.76 <sup>+0.19</sup> <sub>-0.32</sub>	0.58 <sup>+0.27</sup> <sub>-0.29</sub>
118022	9440 ± 270	1.96 ± 0.11	1.44 ± 0.02	2.22 <sup>+0.14</sup> <sub>-0.24</sub>	4.20 <sup>+0.06</sup> <sub>-0.07</sub>	8.50 <sup>+0.30</sup> <sub>-0.45</sub>	0.39 <sup>+0.32</sup> <sub>-0.25</sub>
119213	8620 ± 470	1.99 ± 0.23	1.29 ± 0.04	2.02 <sup>+0.14</sup> <sub>-0.22</sub>	4.14 ± 0.11	8.73 <sup>+0.23</sup> <sub>-0.43</sub>	0.51 ± 0.31
120198	9740 ± 560	2.14 ± 0.26	1.57 ± 0.04	2.37 <sup>+0.17</sup> <sub>-0.25</sub>	4.15 <sup>+0.11</sup> <sub>-0.12</sub>	8.50 <sup>+0.25</sup> <sub>-0.54</sub>	0.47 <sup>+0.31</sup> <sub>-0.33</sub>
124224	12260 ± 480	2.05 ± 0.19	1.93 ± 0.04	3.05 <sup>+0.14</sup> <sub>-0.33</sub>	4.30 <sup>+0.05</sup> <sub>-0.10</sub>	7.63 <sup>+0.69</sup> <sub>-0.51</sub>	0.13 <sup>+0.42</sup> <sub>-0.09</sub>
128898	7760 ± 230	1.85 ± 0.11	1.05 ± 0.01	1.76 <sup>+0.12</sup> <sub>-0.17</sub>	4.15 <sup>+0.06</sup> <sub>-0.07</sub>	8.92 <sup>+0.20</sup> <sub>-0.30</sub>	0.53 <sup>+0.33</sup> <sub>-0.25</sub>
130559	9120 ± 420	2.30 ± 0.25	1.52 ± 0.05	2.26 <sup>+0.16</sup> <sub>-0.23</sub>	4.07 ± 0.10	8.67 <sup>+0.17</sup> <sub>-0.26</sub>	0.62 <sup>+0.25</sup> <sub>-0.26</sub>
137909	7540 ± 420	3.15 ± 0.37	1.46 ± 0.04	2.14 <sup>+0.13</sup> <sub>-0.35</sub>	3.77 <sup>+0.11</sup> <sub>-0.14</sub>	8.91 <sup>+0.16</sup> <sub>-0.07</sub>	0.92 <sup>+0.10</sup> <sub>-0.13</sub>
137949	7370 ± 270	2.16 ± 0.24	1.09 ± 0.07	1.77 <sup>+0.13</sup> <sub>-0.28</sub>	4.02 <sup>+0.08</sup> <sub>-0.12</sub>	9.04 <sup>+0.25</sup> <sub>-0.15</sub>	0.72 <sup>+0.34</sup> <sub>-0.19</sub>
140160	9030 ± 230	2.17 ± 0.15	1.45 ± 0.04	2.19 <sup>+0.15</sup> <sub>-0.23</sub>	4.11 <sup>+0.06</sup> <sub>-0.08</sub>	8.67 <sup>+0.19</sup> <sub>-0.22</sub>	0.56 <sup>+0.26</sup> <sub>-0.21</sub>
140728	9730 ± 550	2.44 ± 0.30	1.69 ± 0.03	2.49 <sup>+0.17</sup> <sub>-0.25</sub>	4.06 <sup>+0.10</sup> <sub>-0.12</sub>	8.56 <sup>+0.17</sup> <sub>-0.27</sub>	0.62 <sup>+0.25</sup> <sub>-0.26</sub>
148112	9170 ± 390	3.34 ± 0.33	1.85 ± 0.06	2.66 <sup>+0.16</sup> <sub>-0.41</sub>	3.81 <sup>+0.09</sup> <sub>-0.11</sub>	8.63 <sup>+0.17</sup> <sub>-0.08</sub>	0.87 <sup>+0.14</sup> <sub>-0.13</sub>
148898	8150 ± 250	2.97 ± 0.19	1.54 ± 0.02	2.25 <sup>+0.13</sup> <sub>-0.35</sub>	3.85 <sup>+0.06</sup> <sub>-0.10</sub>	8.82 <sup>+0.18</sup> <sub>-0.07</sub>	0.86 <sup>+0.15</sup> <sub>-0.11</sub>
151199	8620 ± 390	2.06 ± 0.20	1.32 ± 0.04	2.04 <sup>+0.14</sup> <sub>-0.21</sub>	4.12 ± 0.10	8.74 <sup>+0.21</sup> <sub>-0.34</sub>	0.55 ± 0.28
152107	8840 ± 190	2.30 ± 0.11	1.47 ± 0.03	2.19 <sup>+0.14</sup> <sub>-0.22</sub>	4.06 <sup>+0.05</sup> <sub>-0.06</sub>	8.72 ± 0.16	0.64 <sup>+0.22</sup> <sub>-0.18</sub>

continued on next page

continued from previous page

HD	$T_{\text{eff}}$ (K)	$R$ ( $R_{\odot}$ )	$\log L/L_{\odot}$	$M$ ( $M_{\odot}$ )	$\log(g)_{\text{HRD}}$	$\log t/\text{Gyrs}$	$\tau$
(1)	(2)	(3)	(4)	(5)	(6)	(7)	(8)
170000	$11630 \pm 110$	$3.73 \pm 0.14$	$2.36 \pm 0.04$	$3.56^{+0.04}_{-0.49}$	$3.85^{+0.03}_{-0.07}$	$8.27^{+0.12}_{-0.01}$	$0.88^{+0.09}_{-0.03}$
176232	$7440 \pm 370$	$2.69 \pm 0.30$	$1.30 \pm 0.04$	$1.96^{+0.12}_{-0.40}$	$3.87^{+0.09}_{-0.12}$	$8.99^{+0.24}_{-0.09}$	$0.86^{+0.21}_{-0.15}$
187474	$9900 \pm 400$	$2.56 \pm 0.35$	$1.76 \pm 0.09$	$2.58^{+0.20}_{-0.27}$	$4.03^{+0.10}_{-0.11}$	$8.53^{+0.15}_{-0.21}$	$0.65^{+0.23}_{-0.24}$
188041	$8520 \pm 340$	$2.32 \pm 0.19$	$1.41 \pm 0.04$	$2.11^{+0.14}_{-0.22}$	$4.03 \pm 0.08$	$8.79^{+0.15}_{-0.18}$	$0.67 \pm 0.21$
201601	$7570 \pm 170$	$2.07 \pm 0.12$	$1.10 \pm 0.03$	$1.78^{+0.12}_{-0.17}$	$4.06^{+0.06}_{-0.07}$	$9.00^{+0.13}_{-0.15}$	$0.67^{+0.25}_{-0.18}$
203006	$9240 \pm 480$	$2.35 \pm 0.34$	$1.56 \pm 0.09$	$2.32^{+0.18}_{-0.26}$	$4.06 \pm 0.12$	$8.64^{+0.17}_{-0.28}$	$0.62^{+0.25}_{-0.28}$
217522	$6520 \pm 280$	$1.92 \pm 0.28$	$0.78 \pm 0.09$	$1.48^{+0.13}_{-0.27}$	$4.04^{+0.10}_{-0.16}$	$9.32^{+0.30}_{-0.17}$	$0.86^{+0.49}_{-0.28}$
217831	$6900 \pm 1350$	$2.58 \pm 0.31$	$1.13 \pm 0.14$	$1.79^{+0.12}_{-0.31}$	$3.87^{+0.12}_{-0.14}$	$9.11^{+0.22}_{-0.11}$	$0.88^{+0.23}_{-0.18}$
220825	$9180 \pm 370$	$1.73 \pm 0.14$	$1.28 \pm 0.03$	$2.06^{+0.11}_{-0.22}$	$4.27^{+0.07}_{-0.09}$	$8.36^{+0.48}_{-0.80}$	$0.23^{+0.40}_{-0.20}$
221760	$8470 \pm 230$	$3.62 \pm 0.27$	$1.78 \pm 0.05$	$2.55^{+0.15}_{-0.39}$	$3.73^{+0.07}_{-0.10}$	$8.71^{+0.14}_{-0.05}$	$0.94 \pm 0.09$
223640	$12240 \pm 440$	$2.30 \pm 0.22$	$2.03 \pm 0.05$	$3.17^{+0.20}_{-0.34}$	$4.21^{+0.07}_{-0.10}$	$7.98^{+0.37}_{-0.74}$	$0.32^{+0.35}_{-0.26}$

the spectroscopically-derived  $\log g$  values (referred to as the spectroscopic  $\log g$ ) and therefore, of the derived  $T_{\text{eff}}$  values, we compare with the  $\log g$  values derived from the masses and radii associated with each star’s position on the theoretical HRD (referred to as the HRD  $\log g$ ). We derived spectroscopic surface gravities for 42 of the confirmed mCP stars in the sample and compare these with the HRD  $\log g$  values; the comparison is shown in Fig. 15.

Thirty-seven out of the forty-two (88 per cent) spectroscopic  $\log g$  values are in agreement with the HRD surface gravities within their uncertainties. The discrepancies between the five stars whose spectroscopic and HRD  $\log g$  values are not in agreement range from 7 to 21 per cent. The overall agreement that was yielded by the analysis is to be expected considering the large uncertainties in the spectroscopic  $\log g$  values. This is particularly true of the cooler stars having  $T_{\text{eff}} \lesssim 10\,000$  K, which exhibit median  $\log g$  uncertainties  $\gtrsim 1$  – more than twice that of the hotter stars ( $T_{\text{eff}} > 10\,000$  K) for which the median uncertainty is 0.5. The increase in spectroscopic  $\log g$  uncertainties with decreasing  $T_{\text{eff}}$  reflects a decrease in the sensitivity of the Balmer line profiles to changes in  $\log g$ .

It is apparent from Fig. 15 that the spectroscopic  $\log g$  values are systematically smaller than the HRD  $\log g$  values. There are a number of possible explanations for this discrepancy. It could be related to the choice of evolutionary model grids: if the stars exhibit a metallicity that is systematically higher or lower than the adopted solar value, the HRD  $\log g$  will be affected. Furthermore, the HRD  $\log g$  values are associated with non-rotating models – it is possible that including the rotational velocities of each of the sample mCP stars may serve to reduce this discrepancy. The Lorentz force that exists within the strongly magnetic atmospheres of mCP stars is predicted to modify the pressure stratification (Valyavin, Kochukhov & Piskunov 2004). This effect is manifest in the profiles of H $\alpha$ , H $\beta$ , and H $\gamma$  lines, which may vary over the star’s rotational period for those stars exhibiting field structures that are not symmetric about the star’s rotational axis (e.g. stars hosting dipole fields with non-zero obliquity angles).

Given that the sample consists only of relatively bright stars, effective temperatures of the majority of the confirmed mCP stars have been derived in previously published studies. In particular, both Kochukhov & Bagnulo (2006) (henceforth referred to as KB2006) and Hubrig, North & Schöller (2007) (henceforth referred to as HNS2007) derived  $T_{\text{eff}}$  values for 87 per cent and 58 per cent of the stars in this sample, respectively. We expect the effective temperatures yielded by these studies to be consistent with those derived here considering that all three studies attempt to take into account the presence of chemical peculiarities.

In Fig. 16, we compare the values of  $T_{\text{eff}}$  derived in this study with those derived by KB2006 and HNS2007. We find that 87 per cent and 97 per cent of the effective temperatures derived for the mCP stars included in both this study and those published by KB2006 and HNS2007, respectively, are consistent within their associated uncertainties. HD 38823 exhibits the largest discrepancy ( $12 \pm 5$  per cent) with derived  $T_{\text{eff}}$  values of  $7\,750 \pm 360$  K (this study) and  $6\,900 \pm 210$  K (KB2006); we find that a lower  $T_{\text{eff}}$  of  $7\,350 \pm 800$  K is derived when a solar metallicity is adopted and no chemical

peculiarities or magnetic fields are considered (see Section 5.2.1).

## 6.2 Mass distribution

Based on the comparisons with the evolutionary tracks carried out in Sect. 5.4, we find that the sample’s 52 confirmed mCP stars span a range of masses from 1.48 to  $3.65 M_{\odot}$ . The mass distribution is shown in Fig. 17 (top). Our volume-limited sample is affected by two sources of incompleteness: (1) the completeness of the identified mCP stars is  $\lesssim 80$  per cent for those stars having  $M \lesssim 1.5 M_{\odot}$  and is  $\gtrsim 97$  per cent for stars with  $M \gtrsim 1.9 M_{\odot}$  (Fig. 1); (2) the completeness of the volume-limited sample of stars extracted from the Hipparcos sample increases with mass from  $\sim 87$  per cent to  $\sim 100$  per cent. The mass distribution can be approximately corrected for completeness if the actual incidence rate of mCP stars within individual mass bins is known. We estimated the actual incidence rate by taking the ratio of the number of confirmed mCP stars within each mass bin to the bin’s total number of stars (both mCP and non-mCP) which have been observationally confirmed or rejected as mCP members (see Sect. 4). For instance, in the smallest mass bin ( $1.4 < M/M_{\odot} < 1.8 M_{\odot}$ ) there are 1 063 stars with observational constraints on their mCP status, 968 stars without such constraints, and  $\approx 294$  stars that may be missing from the sample due to the incompleteness of the Hipparcos catalogue. Seven confirmed mCP stars are found in this bin implying an estimated mCP incidence rate of  $7/1\,063 = 0.66 \times 10^{-2}$ ; therefore, we can expect approximately 8 ( $[968 + 294] \times 0.66 \times 10^{-2}$ ) additional mCP stars to be found within the subsample of  $968 + 294 = 1\,262$  stars that have not been confirmed or rejected as mCP members within this mass bin. Applying this estimation to the mass distribution shown in Fig. 17 yields an increase of 8 and 2 stars to the two smallest mass bins; the higher mass bins are unaffected.

The incidence rate of mCP stars as a function of mass can be derived using the masses of both the mCP and non-mCP stars within the sample; this is shown in Fig. 17 (bottom). We find that the fractional incidence increases monotonically from  $0.3 \pm 0.1$  per cent at  $M < 1.8 M_{\odot}$  to approximately 11 per cent at  $3.4 < M/M_{\odot} < 3.8$ . As shown in Fig. 17, correcting for completeness increases the estimated incidence rate in the two smallest mass bins to 0.8 per cent and 0.3 per cent, respectively, while the changes to the higher mass bins are negligible.

As discussed in Fig. 5.4, the metallicities of the mCP stars cannot be confidently determined and, as a result, a relatively large uncertainty is adopted based on the solar neighbourhood ( $Z = 0.014 \pm 0.009$ ; see Sect. 5.4). Accounting for this  $\sigma_Z$ , we find that the uncertainties in mass exhibit median and maximum values of 0.15 and  $0.37 M_{\odot}$ , respectively (4 and 10 per cent of the sample’s mass range of  $1.4 \leq M/M_{\odot} \leq 5$ ). Therefore, we conclude that the properties of both the mCP mass distribution and the fractional incidence rate of mCP stars as a function of mass presented here are likely robust.

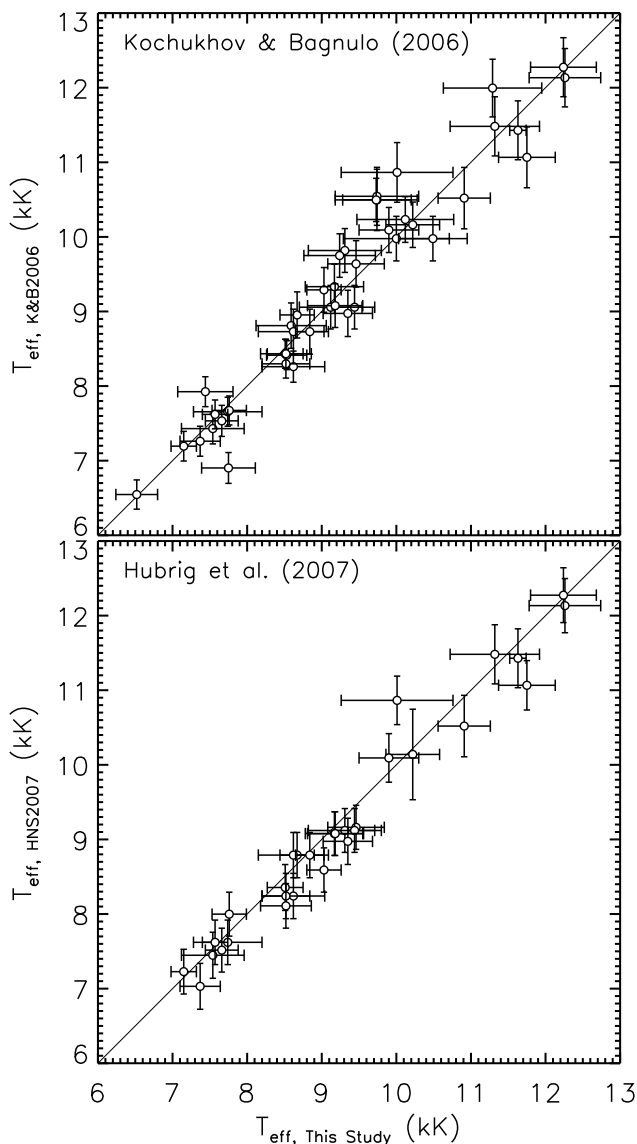


**Figure 16.** Comparison of  $T_{\text{eff}}$  values derived in this study with those derived by Kochukhov & Bagnulo (2006) (top) and Hubrig, North & Schöller (2007) (bottom).

### 6.3 Evolutionary state

Unlike the distribution of masses presented in Sect. 6.2, the absolute ages ( $t_{\text{age}}$ ) and fractional MS ages ( $\tau$ ) derived using theoretical evolutionary tracks vary significantly depending on the adopted metallicity. Furthermore, the uncertainties in  $t_{\text{age}}$  and  $\tau$  are significantly larger for those stars positioned closer to the TAMS compared to the ZAMS as a result of their more rapid evolution (e.g. Kochukhov & Bagnulo 2006; Landstreet et al. 2007). These properties are reflected in the large uncertainties derived in Sect. 5.4.

In Fig. 18 (top), we show the mCP subsample’s distribution of  $\tau$ . The distribution is found to peak near the middle of the MS band at approximately  $\tau = 0.7$ . This is consistent with the  $\tau$  distributions of mCP stars with  $M < 3 M_{\odot}$  reported by KB2006 and HNS2007. These two studies also identified differences in the low-mass ( $M < 3 M_{\odot}$ ) and high-mass ( $M \geq 3 M_{\odot}$ )  $\tau$  distributions; only 7 mCP stars in our

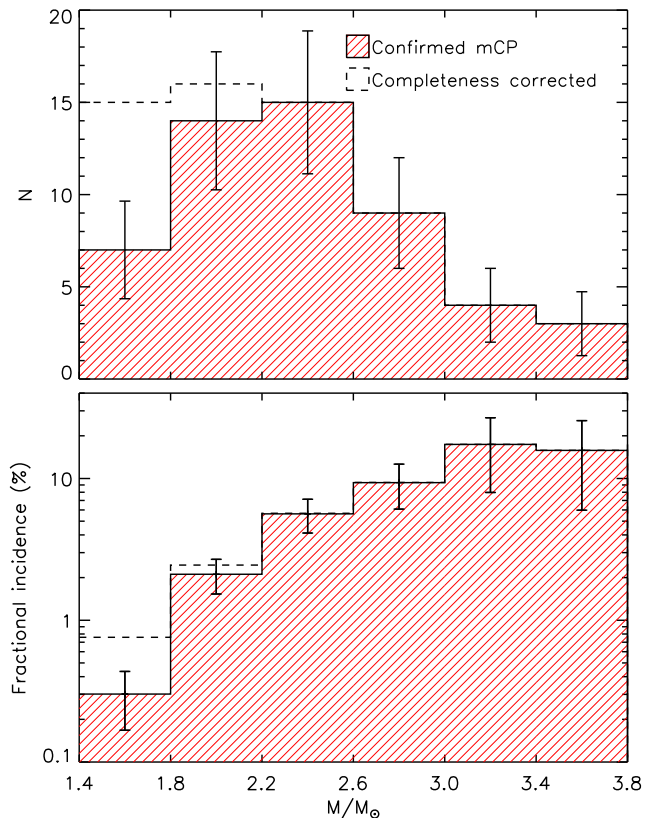


**Figure 17.** *Top:* Distribution of masses of the mCP stars in the sample (red hatched). Correcting for completeness yields the black dashed distribution. *Bottom:* Incidence rate of mCP stars with respect to stellar mass. The large uncertainty associated with the highest mass bin ( $5 < M/M_{\odot} < 5.4$ ) is due to the fact that it contains only three stars. Correcting for completeness increases the incidence rates of the first two bins, as indicated by the black dashed distribution.

sample have  $M \geq 3 M_{\odot}$  and so their  $\tau$  distribution cannot be meaningfully compared with these results.

For the non-mCP stars, the  $\tau$  distribution is characteristically similar to that of the mCP stars. In Fig. 18 (bottom) we show the fractional incidence of mCP stars within the total sample as a function of  $\tau$ . It is evident that the incidence rate is approximately symmetric about  $\tau = 0.6$  increasing from a rate  $\lesssim 0.5$  per cent where  $\tau < 0.2$  and  $\tau > 1$  to a peak rate of  $\approx 2.3$  per cent. We compared the mCP and non-mCP  $\tau$  distributions by computing a Kolmogorov-Smirnov (KS) test statistic, which was found to be 0.16. The significance of this result can be evaluated by estimating the uncertainty in the KS test statistic. The two most important contributions to the uncertainty are likely (1) the relatively small sample size of the mCP sample and (2) the large uncertainties in  $\tau$  that may be attributed to the fact that each star’s metallicity is effectively unknown.

The first of the factors contributing to the uncertainty in the KS test statistic can be evaluated using the case resampling bootstrapping method, which yielded a  $1\sigma$  uncertainty of 0.05. We evaluated the second factor using a Monte Carlo (MC) simulation. This involved generating 1000 mCP and non-mCP  $\tau$  distributions in which, for each star, we add on a random value,  $\Delta\tau$ , that is sampled from the as-

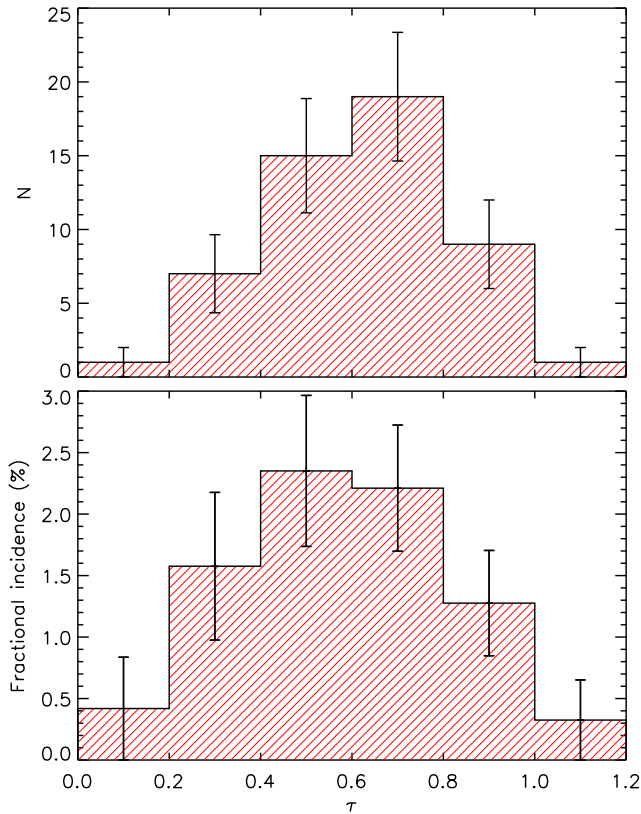


**Figure 18.** *Top:* Distribution of fractional MS ages of the mCP stars in the sample. *Bottom:* Incidence rate of mCP stars with respect to fractional MS age.

sociated  $\tau$  uncertainty (i.e.  $\tau \rightarrow \tau + \Delta\tau$  where  $\Delta\tau$  is randomly drawn from a Gaussian distribution defined by the most probable value and the upper and lower error limits). We then computed the KS test statistic comparing each of the pairs of simulated mCP and non-mCP  $\tau$  distributions. The width of the resulting distribution of test statistics was then interpreted as the approximate uncertainty introduced by the large  $\tau$  uncertainties associated with each star; the MC analysis yielded a  $1\sigma$  uncertainty of 0.07. Combining the two uncertainties estimated from the bootstrapping and MC analyses yields a  $3\sigma$  uncertainty of 0.24. Comparing with the derived KS statistic of 0.16 suggests that the apparent differences between the mCP and non-mCP  $\tau$  distributions is likely not statistically significant.

#### 6.4 Chemical abundances

In Fig. 19, we show mean Fe (top) and Cr (bottom) abundances as a function of  $T_{\text{eff}}$  derived for 45 of the mCP stars. These are compared with the mean abundances and effective temperatures of those 104 stars included in the study published by Ryabchikova (2005) but not included in our volume-limited sample. In general, both data sets appear to be in agreement in terms of the overall trends:  $\log N_{\text{Fe}}/N_{\text{tot}}$  and  $\log N_{\text{Cr}}/N_{\text{tot}}$  tend to increase with  $T_{\text{eff}}$  and reach a peak value at approximately 9500 K. We also compared how the mean Si and Ca abundances derived in both studies vary with  $T_{\text{eff}}$  and find similar agreement: a slight increase

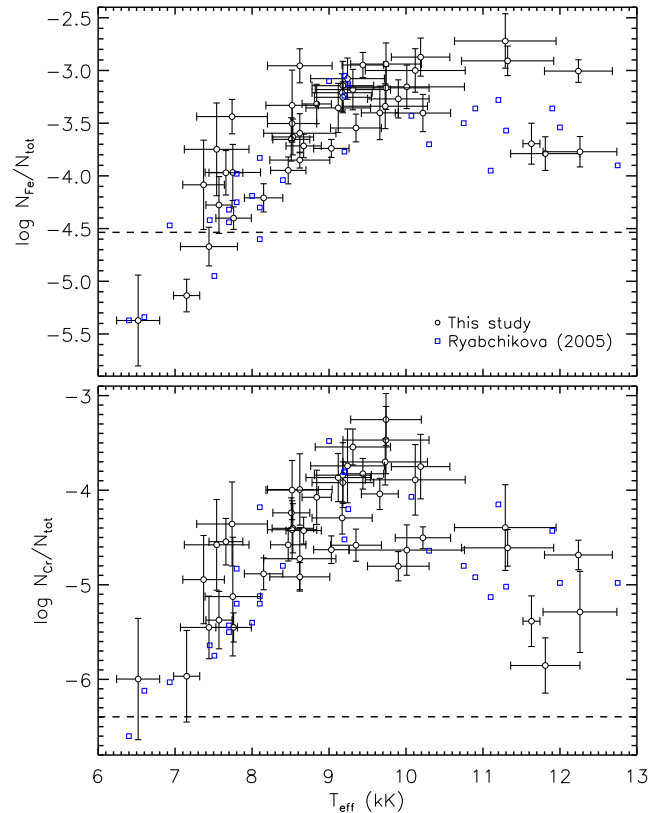


**Figure 19.** Mean Fe (top) and Cr (bottom) abundances as a function  $T_{\text{eff}}$  derived in this study (open black circles) and derived by Ryabchikova (2005) (open blue squares). The horizontal dashed lines correspond to the Fe and Cr solar abundances of  $-4.54$  and  $-6.40$  dex, respectively (Asplund et al. 2009).

in the Si abundances with increasing  $T_{\text{eff}}$  is found while the Ca abundances do not appear strongly correlated with  $T_{\text{eff}}$ . The overall agreement between the Fe, Cr, Si, and Ca abundances derived in this study and those appearing in Ryabchikova (2005) suggests that the final atmospheric parameters (e.g.  $T_{\text{eff}}$ ,  $\log g$ , and abundances) adopted in our sample are reasonably accurate. It is noted that the abundances compiled in their study typically include the effects of magnetic fields (e.g. Ryabchikova et al. 2004).

We were also able to identify correlations between certain chemical abundances and absolute stellar age. In Fig. 20, we show the abundances of Si, Ti, Cr, and Fe for 45 of the mCP stars as a function of  $\log t_{\text{age}}$ . No  $t_{\text{age}}$  error bars are plotted because of the relatively high density of data points and their large error bars which, in some cases, span nearly  $1/3$  of the  $x$ -axis. A best-fitting linear function was calculated for each element using the fitting routine described by Williams, Bureau & Cappellari (2010), which considers errors in both  $x$  and  $y$  coordinates. Symmetric  $\log t_{\text{age}}$  errors were input into the fitting routine by taking the average of the positive and negative error intervals. The statistical significance of each fit was calculated by comparing the  $\chi^2$  values obtained from the first order linear fit with that of a zeroth order fit. The slope ( $m$ ) and significance ( $\sigma$ ) of each fit is shown in Fig. 20.

The linear fits shown in Fig. 20 were found to have slopes ranging from  $m = -3.3$  to  $-1.3$  indicating overall

decreases in the mean abundances with age. Although the significance of the apparent [Ti/H] trend is relatively low at  $0.3\sigma$ , [Si/H], [Cr/H], and [Fe/H] all exhibit statistically significant trends ( $\sigma \geq 4.9$ ). All of the other abundances that were studied – including O, Mg, and S – yielded significance levels  $< 3\sigma$ .

Similar decreases in the mean abundances with age were previously discovered by Bailey, Landstreet & Bagnulo (2014) within a sample of cluster Bp stars. The significance of the [Si/H], [Cr/H], and [Fe/H] trends they reported are lower than those found in this study while they report higher significance levels associated with O, Mg, and Ti. Comparing the slopes of the [Si/H], [Cr/H], and [Fe/H] trends, we find that those derived in this study are significantly steeper; only the linear fits to [Cr/H] derived in both studies exhibit slopes which are in agreement within error. By identifying the stars in our sample having  $T_{\text{eff}} \geq 10^4$  K (i.e. the minimum  $T_{\text{eff}}$  of the stars studied by Bailey, Landstreet & Bagnulo 2014) it is clear that the trends detected in our study are dominated by comparably cooler stars. Furthermore, the hotter stars appear to exhibit mean Cr, Fe, and Ti abundances which deviate from the best-fitting linear trends towards lower abundances. This is confirmed by comparing reduced  $\chi^2$  values associated with the hotter ( $\chi_{\text{hot}}^2$ ) and cooler ( $\chi_{\text{cool}}^2$ ) stars: for [Ti/H], [Cr/H], and [Fe/H],  $\chi_{\text{hot}}^2/\chi_{\text{cool}}^2$  is found to be 2.1, 6.7, and 5.1, respectively. Considering that the minimum age of the cooler stars in our sample corresponds roughly to the maximum age of the hotter stars, it is unclear whether or not the observed deviation in these particular abundances is unique to the hotter stars. A more probable explanation is that the deviations arise from vertical and/or horizontal stratification, which is known to significantly affect both Fe and Cr spectral line profiles (e.g. Bagnulo et al. 2001; Wade et al. 2001b; Kochukhov et al. 2006).

## 7 DISCUSSION AND CONCLUSIONS

The results presented here constitute the first detailed, analytically homogeneous study of the fundamental parameters and chemical abundances of a volume-limited sample of mCP stars. Such a study provides two important and unique contributions to our understanding of mCP stars: (1) it allows for basic conclusions to be drawn while minimizing the observer biases inherent in most previously published surveys; and (2) it comprises of a population of non-mCP stars which can be compared against the sample’s mCP stars. By adopting a distance limit of 100 pc, we are restricted to a stellar population with relatively precise Hipparcos parallax measurements and generally extensive photometric measurements.

The most significant findings presented here are summarized as follows.

- (i) The incidence rate of mCP stars amongst the population of non-mCP stars is found to sharply increase with mass from  $\approx 0.3$  per cent at  $M \approx 1.6 M_{\odot}$  to  $\approx 11$  per cent at  $3 \lesssim M \lesssim 5 M_{\odot}$ . It is noted that this trend is not strongly influenced by sample incompleteness or the uncertainty in metallicity.
- (ii) The mCP stars are more frequently found within the middle of the MS band ( $0.4 < \tau < 0.8$ ) as opposed to near the

ZAMS or the TAMS. This result confirms the findings of Kochukhov & Bagnulo (2006) and Hubrig, North & Schöller (2007), whose studies both used stellar ages derived from the older, less-sophisticated evolutionary models calculated by Schaller et al. (1992) and Schaerer et al. (1993) compared to the newer models calculated by Ekström et al. (2012) and Mowlavi et al. (2012) that are used in this study. Our conclusion is supported by the fact that both the mCP stars’ fractional MS ages and their incidence rates with respect to the non-mCP subsample exhibit similar peaks near  $\tau \approx 0.7$ . However, we note that the relatively small mCP sample size and the large errors in  $\tau$  suggests that the apparent differences to the distributions of mCP and non-mCP  $\tau$  values may not be statistically significant.

- (iii) The mean Cr and Fe abundances appear to decrease with increasing absolute stellar age. Similar trends are found from mean Si and Ti abundances albeit with lower statistical significance levels. The overall trends are consistent with those reported by Bailey, Landstreet & Bagnulo (2014) based on their sample of Bp stars ( $T_{\text{eff}} \geq 10^4$  K); however, the estimated abundance decay rates of Ti, Cr, and Fe are greater. This discrepancy between the derived abundance decay rates may be related to the fact that our sample is predominantly populated by cooler stars: lower abundance decay rates of Cr and Fe associated with the cooler ( $T_{\text{eff}} < 10^4$  K) stars were found compared to those of the hotter ( $T_{\text{eff}} \geq 10^4$  K) stars in our sample.

This paper’s submission date approximately coincides with the second Gaia data release (GDR2) (Gaia Collaboration et al. 2016). GDR2 contains parallax measurements for 49/52 of the mCP stars in our sample. Comparing the reported parallax uncertainties associated with the measurements obtained using Hipparcos and Gaia, we find that the formal uncertainties of the Gaia measurements are typically  $\approx 50$  per cent of the Hipparcos values; however, we find that for 9 out of the 49 stars, the uncertainties associated with the Gaia measurements are larger than those associated with the Hipparcos measurements. Moreover, the two sets of parallax measurements are only in agreement within the reported uncertainties for 22/49 stars (this may not necessarily imply that the distances are also not in agreement, Bailer-Jones et al. 2018). We note that the majority of the mCP stars in our sample (42/52) are brighter than Gaia’s optimal magnitude limit of  $G > 6$  mag. These factors have motivated our decision to not replace the Hipparcos parallax measurements used in the preceding analysis with the GDR2 parallax measurements.

When deriving the masses and ages of both the mCP and non-mCP stars, we adopted a solar metallicity (Asplund et al. 2009) with an uncertainty estimated from the star-to-star variations of F-, G-, and K-type dwarfs within 100 pc ( $[M/H] = 0.0 \pm 0.3$ , as inferred from the catalogue published by Casagrande et al. 2011). However, considering that these low-mass stars are generally expected to be older than the early-F, A-, and late-B-type dwarfs included in this study, there is no reason to expect both populations to exhibit similar metallicity distributions. That is, the older stars may have formed within dramatically different environments compared to those of the younger stars because of (1) the chemical evolution of the solar neighbourhood and (2) the fact that these stars may have originated from

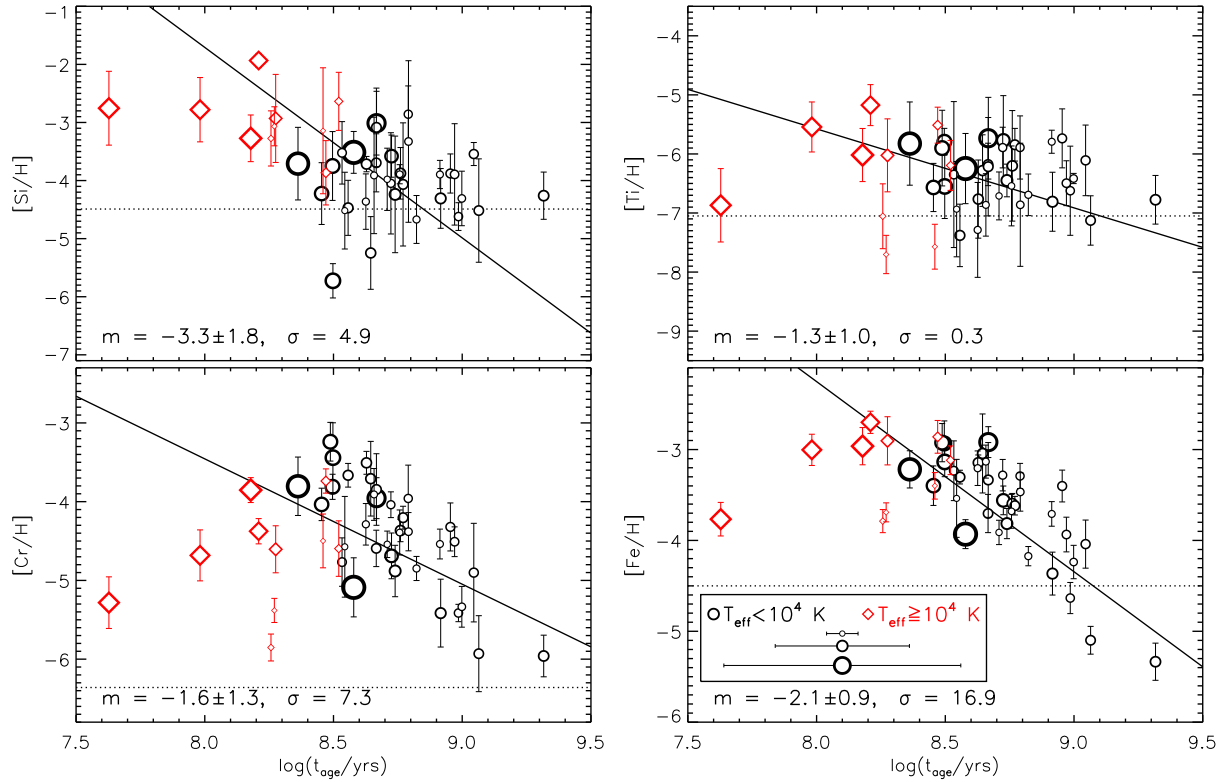


**Figure 20.** Mean Si (top left), Ti (top right), Cr (bottom left), and Fe (bottom right) abundances as a function of absolute stellar age. The sizes of each data point correspond to the widths of the mean uncertainty in  $t_{\text{age}}$  (i.e. half the full width of the error interval); the relation between point size and error bar width is shown in the bottom right panel. The black circles correspond to the cooler stars having  $T_{\text{eff}} < 10^4$  K and the red diamonds correspond to the hotter stars having  $T_{\text{eff}} \geq 10^4$  K. The solid lines correspond to the derived best-fitting linear functions (yielding a slope and fit significance of  $m$  and  $\sigma$ ). The horizontal dotted lines indicate the solar abundances (Asplund et al. 2009) of each element.

further away. In Fig. 16 of Casagrande et al. (2011), the metallicity distributions (in terms of  $[\text{Fe}/\text{H}]$ ) of nearby low-mass stars are divided into old ( $t_{\text{age}} \geq 5$  Gyrs), middle-aged ( $1 \leq t_{\text{age}} \leq 5$  Gyrs), and young ( $t_{\text{age}} < 1$  Gyrs) populations. It is evident that the dispersions of  $[\text{Fe}/\text{H}]$  associated with these sub-populations increase with age suggesting that our adopted  $2\sigma$   $[\text{M}/\text{H}]$  uncertainty – estimated using the full sample – may be somewhat conservative. While this does not discount the possibility of systematic  $[\text{M}/\text{H}]$  biases in our sample of hotter stars, it does provide further evidence that the populations of low- and intermediate-mass stars exhibit characteristically similar metallicities.

Assuming that the Cr and Fe abundance trends are real and not the result of systematic bias, it is somewhat surprising that such a correlation was detected considering the typically large uncertainties derived for  $t_{\text{age}}$ . This may be an indication that the intermediate-mass MS stars within the solar neighbourhood exhibit a lower star-to-star variation in metallicity than was adopted in our analysis. Considering that the derived effective temperatures and luminosities are, in general, consistent with those reported by Kochukhov & Bagnulo (2006) and Hubrig, North & Schöller (2007), such a detection may have been facilitated by the use of the modern, high-density evolutionary model grids calculated by Ekström et al. (2012) and Mowlavi et al. (2012).

We estimate that the completeness of the subsample of mCP stars within 100 pc is largely complete ( $\gtrsim 91$  per cent).

However, our study is not sensitive to those stars which may host ultra-weak fields (e.g. Lignières et al. 2009; Petit et al. 2011a; Blazère et al. 2016) (i.e. no magnetic constraints are obtained for the vast majority of the non-mCP stars). Petit et al. (2011b) report that Vega, which is the first A-type star discovered to host an ultra-weak field, exhibits a complex magnetic field structure (characteristically similar brightness spots were subsequently discovered, Petit et al. 2017). The authors note that the observed field complexity is generally incompatible with the fossil field theory and that Vega’s field – and perhaps all MS A-type stars hosting ultra-weak fields – may have an origin that is distinct from that of the field’s hosted by mCP stars.

The ultra-weak fields detected on the Am stars Sirius A (Petit et al. 2011a),  $\beta$  UMa, and  $\theta$  Leo (Blazère et al. 2016) all exhibit atypical asymmetric circularly polarized Zeeman signatures: the signals have a strong positive lobe and no obvious negative lobe, which differs from the generally symmetric signatures associated with mCP stars. This may suggest that the fields hosted by these stars are similar to Vega – both in terms of their structure and their origin. On the other hand, the ultra-weak Zeeman signature detected on the surface of the Am star Alhena has a symmetric profile that is indistinct from many signatures detected on strongly magnetic mCP stars. This suggests that there may exist a larger population of Am stars that host fields produced by similar processes to those of the mCP stars. At

this point, the connection between the fields hosted by Am stars and those hosted by mCP stars is unclear. We note that no Am stars hosting fields  $\gtrsim 10$  G have been discovered despite repeated searches (e.g. Aurière et al. 2010). If the fields hosted by Am and mCP stars share the same origin (e.g. fossil fields), it is perplexing why they appear to differ so significantly in terms of their strengths.

## ACKNOWLEDGMENTS

GAW acknowledges support in the form of a Discovery Grant from the Natural Science and Engineering Research Council (NSERC) of Canada. We are grateful to Dr. Andrew Tkachenko, Dr. Vadim Tsymbal, and Dr. Colin Folsom for their assistance using the LLMODELS, GSSP, and ZEEMAN LMA codes.

## REFERENCES

- Abt H. A., 1979, *ApJ*, 230, 485  
 Abt H. A., 2001, *AJ*, 122, 2008  
 Abt H. A., Morrell N. I., 1995a, *ApJS*, 99, 135  
 Abt H. A., Morrell N. I., 1995b, *ApJS*, 99, 135  
 Adelman S. J., 1975, *ApJ*, 195, 397  
 Adelman S. J., 1979, *AJ*, 84, 857  
 Alecian E. et al., 2014, *A&A*, 567, A28  
 Alecian G., 2015, *MNRAS*, 454, 3143  
 Alecian G., Stiff M. J., 2010, *A&A*, 516, A53  
 Ammler-von Eiff M., Reiners A., 2012, *A&A*, 542, A116  
 Asplund M., Grevesse N., Sauval a. J., Scott P., 2009, *ARA&A*, 47, 481  
 Aurière M. et al., 2010, *A&A*, 523, A40  
 Aurière M. et al., 2007, *A&A*, 475, 1053  
 Babel J., 1994, *A&A*, 283, 189  
 Bagnulo S., Landstreet J. D., Mason E., Andretta V., Silaj J., Wade G. A., 2006, *A&A*, 450, 777  
 Bagnulo S., Wade G. A., Donati J.-F., Landstreet J. D., Leone F., Monin D. N., Stiff M. J., 2001, *A&A*, 369, 889  
 Bailer-Jones C. A. L., Rybizki J., Fousneau M., Mantelet G., Andrae R., 2018, *ArXiv e-prints*  
 Bailey J. D., Landstreet J. D., Bagnulo S., 2014, *A&A*, 561, A147  
 Balona L. A., 1994, *MNRAS*, 268, 119  
 Bayer C., Maitzen H. M., Paunzen E., Rode-Paunzen M., Sperl M., 2000, *A&AS*, 147, 99  
 Bessell M., Murphy S., 2012, *PASP*, 124, 140  
 Bessell M. S., 2011, *PASP*, 123, 1442  
 Blazère A., Petit P., Lignièrès F., Aurière M., Ballot J., Böhm T., Folsom C. P., Gaurat M., 2016, *A&A*, 586, 1  
 Borra E. F., Landstreet J. D., 1980, *ApJS*, 42, 421  
 Braithwaite J., Cantiello M., 2013, *MNRAS*, 428, 2789  
 Braithwaite J., Nordlund A., 2006, *A&A*, 450, 1077  
 Brown A. G. A., Verschueren W., 1997, *A&A*, 319, 811  
 Casagrande L., Schönrich R., Asplund M., Cassisi S., Ramírez I., Meléndez J., Bensby T., Feltzing S., 2011, *A&A*, 530, A138  
 Charbonneau P., 2005, *Living Rev. Sol. Phys.*, 2  
 Charbonneau P., MacGregor K. B., 2001, *ApJ*, 559, 1094  
 Cohen M., Wheaton W. A., Megeath S. T., 2003, *AJ*, 126, 1090  
 Cowley A., 1973, *PASP*, 85, 314  
 Cowley A., Cowley C., Jaschek M., Jaschek C., 1969, *AJ*, 74, 375  
 Cowling T. G., 1945, *MNRAS*, 105, 166  
 Cramer N., 1999, *New Astron. Rev.*, 43, 343  
 Cucchiaro A., Jaschek M., Jaschek C., Macau-Hercot D., 1976, *A&AS*, 26, 241  
 Cucchiaro A., Jaschek M., Jaschek C., Macau-Hercot D., 1980, *A&AS*, 40, 207  
 Cucchiaro A., Macau-Hercot D., Jaschek M., Jaschek C., 1977, *A&AS*, 30, 71  
 Cucchiaro A., Macau-Hercot D., Jaschek M., Jaschek C., 1978a, *A&AS*, 33, 15  
 Cucchiaro A., Macau-Hercot D., Jaschek M., Jaschek C., 1978b, *A&AS*, 35, 75  
 Davison A., Hinkley D., 1997, *Bootstrap Methods and Their Application*, Cambridge Series in Statistical and Probabilistic Mathematics. Cambridge University Press  
 Donati J.-F., Landstreet J., 2009, *ARA&A*, 47, 333  
 Donati J.-F., Semel M., Carter B. D., Rees D. E., Cameron A. C., 1997, *MNRAS*, 291, 658  
 Ducati J. R., 2002, *VizieR Online Data Catalog*, 2237  
 Duez V., Mathis S., 2010, *A&A*, 517, 1  
 Ekström S. et al., 2012, *A&A*, 537, 1  
 ESA, ed., 1997, *ESA Special Publication*, Vol. 1200, The HIPPARCOS and TYCHO catalogues. Astrometric and photometric star catalogues derived from the ESA HIPPARCOS Space Astrometry Mission  
 Esteban C., Peimbert M., García-Rojas J., Ruiz M. T., Peimbert A., Rodríguez M., 2004, *MNRAS*, 355, 229  
 Folsom C. P., Bagnulo S., Wade G. A., Alecian E., Landstreet J. D., Marsden S. C., Waite I. A., 2012, *MNRAS*, 422, 2072  
 Francis C., 2013, *MNRAS*, 436, 1343  
 Francis C., 2014, *MNRASL*, 444, L6  
 Gaia Collaboration et al., 2016, *A&A*, 595, A1  
 Georgy C., Ekström S., Granada a., Meynet G., Mowlavi N., Eggenberger P., Maeder a., 2013, *A&A*, 553, 1  
 Golay M., 1972, *Vistas Astron.*, 14, 13  
 Gray D., 2005, *The Observation and Analysis of Stellar Photospheres*. Cambridge University Press  
 Hauck B., Mermilliod M., 1997, *VizieR Online Data Catalog*, 2215  
 Hauck B., North P., 1982, *A&A*, 114, 23  
 Hauck B., North P., 1993, *A&A*, 269, 403  
 Hoffleit D., Jaschek C., 1991, *The Bright star catalogue*  
 Hoffleit D., Warren, Jr. W. H., 1995, *VizieR Online Data Catalog*, 5050  
 Hubrig S., North P., Schöller M., 2007, *Astron. Nachrichten*, 328, 475  
 Jaschek M., Jaschek C., 1980, *A&AS*, 42, 115  
 Khalack V. R., Wade G. A., 2006, *A&A*, 450, 1157  
 Kochukhov O., Bagnulo S., 2006, *A&A*, 450, 763  
 Kochukhov O., Drake N. A., Piskunov N., de la Reza R., 2004, *A&A*, 424, 935  
 Kochukhov O., Khan S., Shulyak D., 2005, *A&A*, 433, 671  
 Kochukhov O., Landstreet J. D., Ryabchikova T., Weiss W. W., Kupka F., 2002, *MNRAS*, 337, 1  
 Kochukhov O., Rusomarov N., Valenti J. A., Stempels H. C., Snik F., Rodenhuis M., Piskunov N., 2015, *A&A*, 574, 1  
 Kochukhov O., Ryabchikova T. A., 2017, *MNRAS*, 474,

- 2787  
 Kochukhov O., Silvester J., Bailey J. D., Landstreet J. D., Wade G. A., 2017, *A&A*, 605, 1  
 Kochukhov O., Sudnik N., 2013, *A&A*, 554, 1  
 Kochukhov O., Tsymbal V., Ryabchikova T., Makaganyk V., Bagnulo S., 2006, *A&A*, 460, 831  
 Kodaira K., 1969, *ApJ*, 157, L59  
 Künzli M., North P., Kurucz R. L., Nicolet B., 1997, *A&AS*, 122, 51  
 Kupka F., Paunzen E., Maitzen H. M., 2003, *MNRAS*, 341, 849  
 Kupka F. G., Ryabchikova T. A., Piskunov N. E., Stempels H. C., Weiss W. W., 2000, *Balt. Astron.*, 9, 590  
 Landstreet J. D., 1982, *ApJ*, 258, 639  
 Landstreet J. D., 1988, *ApJ*, 326, 967  
 Landstreet J. D., 1992, *Astron. Astrophys. Rev.*, 4, 35  
 Landstreet J. D., Bagnulo S., Andretta V., Fossati L., Mason E., Silaj J., Wade G. A., 2007, *A&A*, 698, 685  
 Landstreet J. D., Mathys G., 2000, *A&A*, 359, 213  
 LeBlanc F., Monin D., 2004, *Proc. Int. Astron. Union*, 224, 193  
 Leblanc F., Monin D., Hauschildt P. H., 2009, *A&A*, 944, 937  
 Lignières F., Petit P., Böhm T., Aurière M., 2009, *A&A*, 500, L41  
 Lutz T. E., Kelker D. H., 1973, *PASP*, 85, 573  
 Maitzen H. M., 1976, *A&A*, 51, 223  
 Maitzen H. M., Pressberger R., Paunzen E., 1998, *A&AS*, 128, 573  
 Maitzen H. M., Vogt N., 1983, *A&A*, 123, 48  
 Maitzen H. M., Weiss W. W., Wood H. J., 1980, *A&A*, 81, 323  
 Masana E., Jordi C., Maitzen H., Torra J., 1998, *A&AS*, 128, 265  
 Mermilliod J.-C., Mermilliod M., Hauck B., 1997, *A&AS*, 124, 349  
 Michaud G., 1970, *ApJ*, 160, 641  
 Michaud G., 1980, *AJ*, 85, 589  
 Michaud G., Charland Y., Vauclair S., Vauclair G., 1976, *ApJ*, 210, 447  
 Mignard F., 2000, *A&A*, 354, 522  
 Molenda-Zakowicz J., Polubek G., 2004, *Acta Astron.*, 54, 281  
 Moss D., 2003, *A&A*, 403, 693  
 Moss D., 2004, in *Proc. IAU Symp. No. 224 No. 224*, pp. 245–252  
 Mowlavi N., Eggenberger P., Meynet G., Ekström S., Georgy C., Maeder A., Charbonnel C., Eyer L., 2012, *A&A*, 541, A41  
 Neiner C., Alecian E., 2013, in *EAS Publications Series*, Vol. 64, *EAS Publications Series*, Pavlovski K., Tkachenko A., Torres G., eds., pp. 75–79  
 Neiner C., Wade G. A., Marsden S. C., Blazère A., 2017, in *Second BRITe-Constellation Science Conference: Small satellites-big science*, *Proceedings of the Polish Astronomical Society volume 5*, held 22-26 August, 2016 in Innsbruck, Austria. Edited by Konstanze Zwintz and Ennio Poretti. Polish Astronomical Society, Bartycka 18, 00-716 Warsaw, Poland, pp.86-93, Zwintz K., Poretti E., eds., pp. 86–93  
 Netopil M., Paunzen E., Hümmelich S., Bernhard K., 2017, *MNRAS*, 468, 2745  
 Nordström B. et al., 2004, *A&A*, 418, 989  
 Paunzen E., Maitzen H. M., 2005, *A&A*, 441, 631  
 Perryman M. A. C. et al., 1997, *A&A*, 323, L49  
 Petit P., Hébrard E. M., Böhm T., Folsom C. P., Lignières F., 2017, *MNRAS*, 472, L30  
 Petit P. et al., 2011a, *A&A*, 532, 1  
 Petit P., Lignières F., Wade G. A., Aurière M., Alina D., Böhm T., Oza A., 2011b, *Astron. Nachrichten*, 332, 943  
 Pilachowski C. A., Bonsack W. K., Wolff S. C., 1974, *A&A*, 37, 275  
 Piskunov N. E., Kupka F., Ryabchikova T. A., Weiss W. W., Jeffery C. S., 1995, *A&AS*, 112, 525  
 Pourbaix D., Jorissen A., 2000, *A&AS*, 145, 161  
 Power J., 2007, Master's thesis, Queen's University, Canada  
 Przybilla N., Nieva M.-F., Butler K., 2008, *ApJ*, 688, L103  
 Reiners A., Schmitt J. H. M. M., 2003, *A&A*, 398, 647  
 Renson P., Gerbaldi M., Catalano F. A., 1991, *A&AS*, 89, 49  
 Renson P., Manfroid J., 2009, *A&A*, 498, 961  
 Rice J. B., Wehlau W., 1990, *A&A*, 233, 503  
 Royer F., Grenier S., Zorec J., 2002, 911, 897  
 Rufener F., Nicolet B., 1988, *A&A*, 206, 357  
 Rusomarov N., Kochukhov O., Ryabchikova T., Piskunov N., 2015, *A&A*, 573, A123  
 Ryabchikova T., Kochukhov O., Bagnulo S., 2008, *A&A*, 480, 811  
 Ryabchikova T., Leone F., Kochukhov O., 2005, *A&A*, 438, 973  
 Ryabchikova T., Nesvacil N., Weiss W. W., Kochukhov O., Stütz C., 2004, *A&A*, 423, 705  
 Ryabchikova T., Piskunov N., Kurucz R. L., Stempels H. C., Heiter U., Pakhomov Y., Barklem P. S., 2015, *Phys. Scr.*, 90  
 Ryabchikova T., Wade G., Aurière M., 2005, *A&A*, 429, 55  
 Ryabchikova T. A., 2005, *Astron. Lett.*, 31, 437  
 Ryabchikova T. A., Adelman S. J., Weiss W. W., Kuschnig R., 1997, *A&A*, 322, 234  
 Sargent W. L. W., Searle L., 1967, in *Magnetic and Related Stars*, Cameron R. C., ed., p. 209  
 Schaerer D., Meynet G., Maeder A., Schaller G., 1993, *A&AS*, 98, 523  
 Schaller G., Schaerer D., Meynet G., Maeder A., 1992, *A&AS*, 96, 269  
 Shorlin S. L. S., Wade G. A., Donati J.-F., Landstreet J. D., Petit P., Sigut T. A. A., Strasser S., 2002, *A&A*, 392, 637  
 Shulyak D., Tsymbal V., Ryabchikova T., Stütz C., Weiss W., 2004, *A&A*, 428, 993  
 Silvester J., Kochukhov O., Wade G. A., 2015, *MNRAS*, 453, 2163  
 Skiff B. A., 2014, *VizieR Online Data Catalog*, 1  
 Stepień K., 1978, *A&A*, 70, 509  
 Stepień K., 1994, in *Chem. peculiar Magn. Stars*, Zverko J., Ziznovsky J., eds., *Tatranska Lomnica*, Slovak Republic, p. 8  
 Stibbs D. W. N., 1950, *MNRAS*, 110, 395  
 Stift M. J., Alecian G., 2016, *MNRAS*, 457, 74  
 Tkachenko A., 2015, *A&A*, 581, 1  
 Trumpler R., Weaver H., 1953, *Statistical Astronomy*. Dover  
 Valenti J. A., Piskunov N. E., 1996, in *Model Atmos. Spectr. Synth.*, pp. 175–179

- Valyavin G., Kochukhov O., Piskunov N., 2004, *A&A*, 420, 993
- van Leeuwen F., 2007, *A&A*, 474, 653
- Vergely J.-L., Ferrero R. F., Egret D., Köeppen J., 1998, *A&A*, 340, 543
- Vogt N., Kerschbaum F., Maitzen H., Faundez-Abans M., 1998, *A&AS*, 130, 455
- Wade G. A., Bagnulo S., Kochukhov O., Landstreet J. D., Piskunov N., Stift M. J., 2001a, *A&A*, 374, 265
- Wade G. a., Donati J.-F., Landstreet J. D., Shorlin S. L. S., 2000, *MNRAS*, 313, 823
- Wade G. A., Ryabchikova T. A., Bagnulo S., Piskunov N., 2001b, in *ASP Conf. Ser.*
- Waelkens C., Aerts C., Kestens E., Grenon M., Eyer L., 1998, *A&A*, 330, 215
- Williams M. J., Bureau M., Cappellari M., 2010, *MNRAS*, 409, 1330
- Wilson R. et al., 1972, *Nature*, 238, 34
- Wraight K. T., Fossati L., Netopil M., Paunzen E., Rode-Paunzen M., Bewsher D., Norton A. J., White G. J., 2012, *MNRAS*, 420, 757
- Yakunin I. et al., 2015, *MNRAS*, 447, 1418
- Young A., Martin A. E., 1973, *ApJ*, 181, 805
- Zorec J., Cidale L., Arias M. L., Frémat Y., Muratore M. F., Torres A. F., Martayan C., 2009, *A&A*, 501, 297
- Zorec J., Royer F., 2012, *A&A*, 537, A120

**Table 4.** Derived chemical abundances for the 45/52 mCP stars in the sample with available spectroscopic measurements.

HD	[Si/H]	[Ti/H]	[Cr/H]	[Fe/H]
3980	$-3.01 \pm 0.36$	$-5.73 \pm 0.59$	$-3.96 \pm 0.37$	$-2.92 \pm 0.16$
11502	$-3.27 \pm 0.62$	$-6.02 \pm 0.70$	$-3.85 \pm 0.37$	$-2.96 \pm 0.20$
15089	$-3.87 \pm 0.55$	$-6.20 \pm 0.69$	$-4.37 \pm 0.26$	$-3.59 \pm 0.17$
15144	$-4.07 \pm 0.40$	$-5.84 \pm 0.45$	$-4.20 \pm 0.16$	$-3.62 \pm 0.20$
18296	$-2.64 \pm 0.41$	$-6.19 \pm 0.41$	$-4.60 \pm 0.26$	$-3.12 \pm 0.20$
24712	$-4.52 \pm 0.89$	$-7.13 \pm 0.42$	$-5.93 \pm 0.48$	$-5.10 \pm 0.15$
27309	$-1.93 \pm 0.51$	$-5.17 \pm 0.50$	$-4.38 \pm 0.43$	$-2.70 \pm 0.24$
29305	$-3.27 \pm 0.36$	$-7.06 \pm 0.76$	$-5.85 \pm 0.29$	$-3.79 \pm 0.16$
38823	$-3.51 \pm 0.20$	$-6.25 \pm 0.60$	$-5.09 \pm 0.63$	$-3.93 \pm 0.26$
40312	$-3.14 \pm 0.24$	$-7.57 \pm 0.75$	$-4.50 \pm 0.11$	$-3.40 \pm 0.17$
56022	$-4.22 \pm 0.59$	$-6.57 \pm 0.23$	$-4.03 \pm 0.16$	$-3.40 \pm 0.25$
62140	$-3.88 \pm 0.30$	$-5.74 \pm 0.54$	$-4.32 \pm 0.44$	$-3.40 \pm 0.16$
65339	$-3.33 \pm 0.34$	$-6.86 \pm 0.50$	$-4.38 \pm 0.30$	$-3.47 \pm 0.18$
72968	$-3.72 \pm 0.87$	$-6.76 \pm 0.38$	$-3.51 \pm 0.19$	$-3.14 \pm 0.19$
74067	$-3.87 \pm 1.00$	$-5.51 \pm 0.28$	$-3.74 \pm 0.33$	$-2.86 \pm 0.17$
83368	$-3.89 \pm 0.53$	$-6.50 \pm 0.64$	$-4.51 \pm 0.25$	$-3.93 \pm 0.21$
96616	$-3.91 \pm 0.47$	$-6.86 \pm 0.41$	$-3.91 \pm 0.21$	$-3.13 \pm 0.22$
108662	-	$-5.90 \pm 0.09$	$-3.24 \pm 0.26$	$-2.92 \pm 0.18$
108945	$-3.89 \pm 0.44$	$-6.54 \pm 0.94$	$-4.39 \pm 0.14$	$-3.68 \pm 0.11$
112185	$-4.52 \pm 0.12$	$-6.93 \pm 0.35$	$-4.57 \pm 0.16$	$-3.54 \pm 0.12$
112413	$-2.93 \pm 0.24$	$-6.02 \pm 0.20$	$-4.60 \pm 0.19$	$-2.90 \pm 0.14$
118022	$-3.75 \pm 1.06$	$-5.79 \pm 0.28$	$-3.81 \pm 0.15$	$-2.93 \pm 0.10$
119213	$-3.58 \pm 0.64$	$-5.77 \pm 0.62$	$-4.69 \pm 0.33$	$-3.56 \pm 0.18$
120198	$-5.73 \pm 0.55$	$-6.55 \pm 0.42$	$-3.44 \pm 0.32$	$-3.14 \pm 0.17$
124224	$-2.75 \pm 0.49$	$-6.87 \pm 0.53$	$-5.28 \pm 0.42$	$-3.77 \pm 0.14$
128898	$-4.31 \pm 0.41$	$-6.81 \pm 0.35$	$-5.42 \pm 0.15$	$-4.36 \pm 0.11$
130559	$-3.08 \pm 0.50$	$-6.22 \pm 0.36$	$-3.85 \pm 0.23$	$-3.33 \pm 0.21$
137909	$-3.90 \pm 0.63$	$-5.79 \pm 0.61$	$-4.54 \pm 0.47$	$-3.71 \pm 0.43$
137949	$-3.54 \pm 0.68$	$-6.11 \pm 0.83$	$-4.90 \pm 0.45$	$-4.04 \pm 0.41$
140160	$-3.69 \pm 0.13$	$-6.18 \pm 0.66$	$-4.59 \pm 0.15$	$-3.70 \pm 0.09$
140728	$-4.47 \pm 1.39$	$-7.38 \pm 1.04$	$-3.66 \pm 0.24$	$-3.30 \pm 0.21$
148112	$-4.36 \pm 0.87$	$-7.29 \pm 0.34$	$-4.29 \pm 0.16$	$-3.21 \pm 0.17$
148898	$-4.67 \pm 0.54$	$-6.69 \pm 0.41$	$-4.85 \pm 0.17$	$-4.17 \pm 0.13$
151199	$-4.24 \pm 0.47$	$-6.45 \pm 0.53$	$-4.88 \pm 0.15$	$-3.81 \pm 0.08$
152107	$-4.05 \pm 0.16$	$-5.89 \pm 0.68$	$-4.04 \pm 0.29$	$-3.28 \pm 0.19$
170000	$-3.07 \pm 0.48$	$-7.70 \pm 0.80$	$-5.38 \pm 0.26$	$-3.69 \pm 0.19$
176232	$-4.62 \pm 1.00$	$-6.62 \pm 0.53$	$-5.41 \pm 0.33$	$-4.63 \pm 0.18$
187474	$-3.52 \pm 0.55$	$-6.35 \pm 0.30$	$-4.77 \pm 0.15$	$-3.23 \pm 0.18$
188041	$-2.86 \pm 0.54$	$-5.89 \pm 1.24$	$-3.96 \pm 0.31$	$-3.29 \pm 0.33$
201601	$-4.31 \pm 0.76$	$-6.42 \pm 0.62$	$-5.33 \pm 0.30$	$-4.24 \pm 0.27$
203006	$-5.25 \pm 0.50$	$-6.28 \pm 0.42$	$-3.71 \pm 0.35$	$-3.04 \pm 0.16$
217522	$-4.26 \pm 0.66$	$-6.78 \pm 0.81$	$-5.96 \pm 0.64$	$-5.33 \pm 0.43$
220825	$-3.71 \pm 1.08$	$-5.82 \pm 0.38$	$-3.80 \pm 0.34$	$-3.22 \pm 0.15$
221760	$-3.98 \pm 0.47$	$-6.71 \pm 0.55$	$-4.54 \pm 0.17$	$-3.91 \pm 0.13$
223640	$-2.78 \pm 0.34$	$-5.54 \pm 0.32$	$-4.68 \pm 0.15$	$-3.00 \pm 0.10$